Project No. 13-4855

BiI_3 Gamma-Ray Spectrometers for Reliable Room Temperature Nuclear Materials Safeguarding

Fuel Cycle Research and Development

Juan C. Nino
University of Florida

Dan Vega, Federal POC
Mike Miller, Technical POC

NEUP Nuclear Energy University Programs
U.S. Department of Energy

Final Report of DOE/IUP Grant: DE-NE0000730

BiI_3 Gamma-Ray Spectrometers for Reliable Room Temperature Nuclear Materials Safeguarding

by

Juan C. Nino (Principal Investigator), James Baciak (Co-Principal Investigator), Paul Johns, Soumitra Sulekar, James Totten, and Jyothir Nimmagadda.

University of Florida
Department of Materials Science and Engineering
Gainesville, FL 32611
(352) 846-3787, Fax: (352) 846-3355, jnino@ufl.edu

June 1st 2014 – January 1st 2017

Main Results from Project

BiI_3 had been investigated for its unique properties as a layered compound semiconductor for many decades. However, despite the exceptional atomic, physical, and electronic properties of this material, good resolution gamma ray spectra had never been reported for BiI_3. The shortcomings that previously prevented BiI_3 from reaching success as a gamma ray sensor were, through this project, identified and suppressed to unlock the performance of this promising compound. Included in this work were studies on a number of methods which have, for the first time, enabled BiI_3 to exhibit spectral performance rivaling many other candidate semiconductors for room temperature gamma ray sensors. New approaches to crystal growth were explored that allow BiI_3 spectrometers to be fabricated with up to 2.2% spectral resolution at 662 keV. Fundamental studies on trap states, dopant incorporation, and polarization were performed to enhance performance of this compound. Additionally, advanced detection techniques were applied to display the capabilities of high quality BiI_3 spectrometers. Overall, through this work, BiI_3 has been revealed as a potentially transformative material for nuclear security and radiation detection sciences.

Contents

Summary of Efforts

The following sections summarize the most notable achievements made during this work for the 13 project objectives. Major individual highlights include:

- Sb:BiI_3 single crystals were synthesized with radiation sensitive active volumes of approximately 1 cm^3.
- Resolution of 2.2% at 662 keV has been demonstrated in spectrometers fabricated with Sb:BiI_3 sensors.
- The capability of pixelated and Frisch collar BiI_3 spectrometers to produce radiation spectra has been shown, and additionally, initial attempts at applying depth correction to BiI_3 were made.
- Performance-limiting void inclusion defects were discovered to populate the bulk of BiI_3 grown via the nominal Bridgman method.
- The development of modified crystal growth methods has led to a dramatic reduction of void inclusion concentrations in BiI_3 crystals, and has yielded spectrometers with larger active volumes and crystallographic quality than has ever before been reported.
- The processing of BiI_3 was optimized to produce IC-substrate integrated detectors with better resistivity and leakage current values than ever before reported for the compound.
- Detailed studies on the incorporation of impurities and the Sb dopant into the BiI_3 lattice has provided better strategies for defect engineering BiI_3, as well as fundamentally a deeper understanding of dopants in layered structure semiconductors.
- The characterization of band gap trap states has led to the first determination of capture cross sections and ionization energy levels for Sb-doped BiI_3.
- The thorough examination of polarization phenomena in BiI_3 led to the understanding that anion migration under electric fields is the predominant mechanism causing polarization.
- The performance degradation of BiI_3 in mixed gamma-neutron fields was characterized using the University of Florida Training Reactor.
- Measurements of used nuclear fuel were collected with BiI_3 spectrometers, side-by-side with commercial CZT, to analyze performance.

Objective 1: Growth of Doped-BiI_3 Large Single Crystals

Throughout this work, single crystals of BiI_3 were grown via the Bridgman-Stockbarger vertical gradient freeze ("Bridgman") method of crystal growth. Both conventional growth as developed in the works of Qiu [1], as well as Bridgman growth modified by a superheating gradient [2], were utilized to produce single crystal BiI_3 boules. Typical growth parameters involved ~40 g charges of BiI_3 powder loaded into 17 mm inner diameter Pyrex ampoules with custom designed pointed tips. The focus of crystal growth in this work was not just to grow BiI_3 in arbitrarily large volumes, but to produce crystal boules that maximized the "active volume" of a detector. The "active volume" is the most important physical parameter to consider toward the detection efficiency of an RTSD. Active volume refers to the volume within the crystal that, if a gamma ray were to interact within it, would allow a complete induction of charge from the interaction. Through crystal growth and processing techniques, it is crucial to reduce the concentrations of both microscopic and atomistic defects within a crystal boule such that the active volume of a detector is maximized and the spectrometer can exhibit good detection efficiency. A flow chart outlining the methodology used in this work to prepare BiI_3 spectrometers is presented in Figure 1.

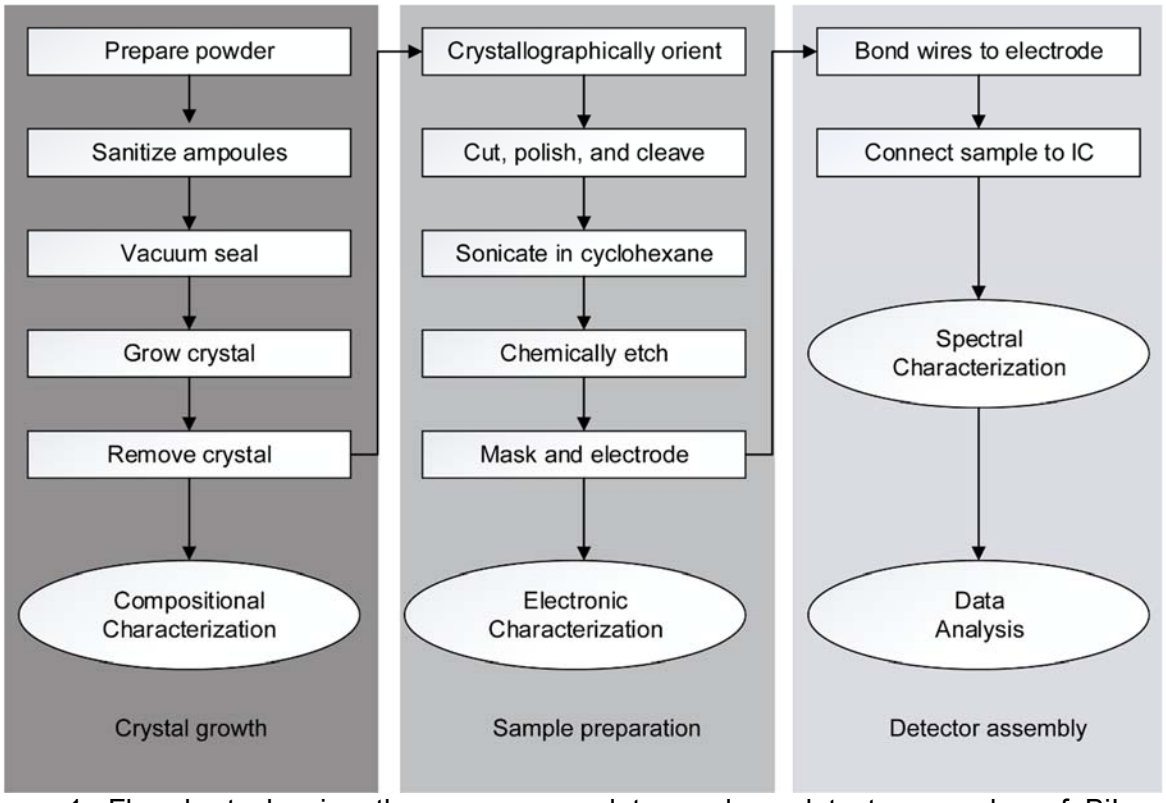

Figure 1. Flowchart showing the process used to produce detector samples of BiI_3 with maximized active volumes.

Examples of BiI_3 boules grown from the modified Bridgman method developed through this project are shown in Figure 2. In many cases, the entirety of the BiI_3 boule is not a single crystal phase. Particularly in the first-to-freeze (bottom of crystal) region, several grains may be present. However, there are large regions in the bulk where single phases exist with volumes on the order of 2-3 cm^3. From these regions, single crystal samples were extracted for fabrication into spectrometers. The largest BiI_3 detectors produced in this work exhibited volumes approximately 1.0 - 1.1 cm^3. Examples of BiI_3 single crystals cut and polished into spectrometer-grade samples, prior to electrode deposition, are shown in Figure 3.

Figure 2: Ingots of BiI_3 grown through the Bridgman method with superheat gradient modifications.

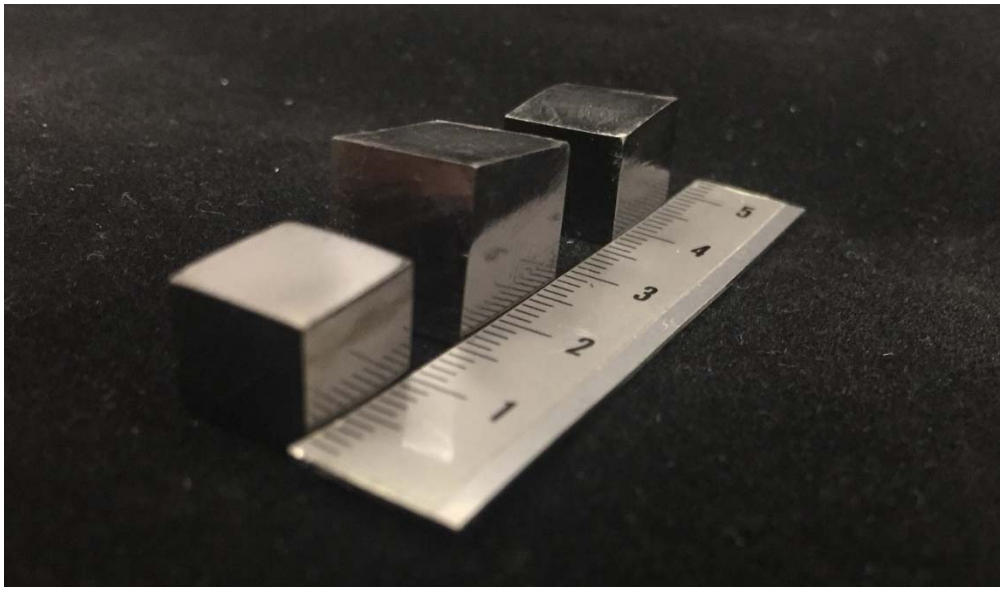

Figure 3: Large single crystals of BiI_3 cut and polished for preparation as radiation detectors.

Objective 2: Crystallographic and Compositional Characterization of Grown Crystals

Crystallographic Characterization

Regions of a semiconductor crystal that feature high concentrations of defects or damage will not allow charge induced from gamma ray ionization to be detected in a spectrometer. Identifying and understanding structural defects in single crystals is crucial to improving the active volume and electronic properties of RTSD compounds. Considering the well-developed material CdZnTe (CZT), in even the highest quality crystals, precipitates, secondary phases, defects from processing, and atomistic defects from stoichiometry deviations or impurities remain significantly deleterious to the material's performance as a detector [3-8]. It is critical to thoroughly understand if such defects exist in BiI_3 early in the development of this material. Crystallographic characterization of BiI_3 samples is therefore extremely important toward the engineering of better sensor crystals.

Through this work the first evidence of major structural defects, in the form of void inclusions, within BiI_3 and Sb:BiI_3 single crystals have been presented. The presence of the void inclusions were discovered through infrared (IR) microscopy performed at Pacific Northwest National Lab. Figure 4 shows several of these IR micrographs, emphasizing the remarkably geometric shapes that the voids take. It was discovered that there was a strong correlation between the concentration of void inclusions in a sample of BiI_3 and its ability to produce a radiation spectra. Samples that exhibited no response to radiation were discovered to have bulks that were full of void inclusions. Likewise, samples that were able to respond to radiation sources were found to contain sparse concentrations of voids. Based on this finding, priority of the project in FY'14 was shifted to suppressing the formation of the voids in order to improve the active volume and detection capabilities of BiI_3 detectors.

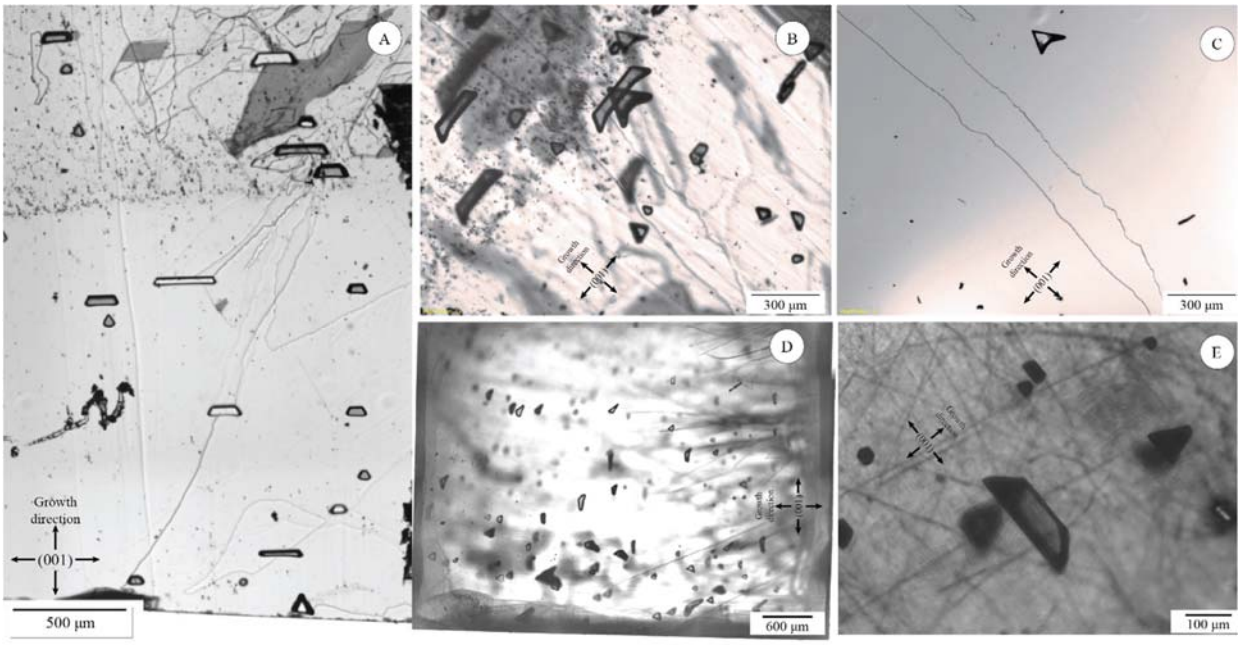

Figure 4: Highly geometric voids are found in samples of Bridgman-grown BiI_3 and Sb-doped BiI_3

The highly geometric nature of the void inclusions gave evidence that they arose as an artifact of some phenomena related to disturbances during crystallization. The trigonal pyramidal and truncated trigonal prism shapes, orientated along the basal plane of the crystal in every sample, implied that some disturbance in the regular stacking order of the crystal during growth were “seeding” their presence. Crystallographic defects in some compounds have been shown to be related to the quality of the “mother” phase of the compound [9]. This occurs because in strongly ionic compounds, even at temperatures past the melting point, there can remain ionically bound aggregates of a solid phase floating within the melt. When the molten phase begins to crystallize, these aggregates serve as nucleation sites for secondary gains, precipitates, or similar crystallographic defects. However, by introducing mass flow into the melt, these ionic aggregates have been shown to further dissolve and improve the quality of the crystallized phase. This has been proven in the compounds CdTe and AgGaTe by introducing mass flow through a convection-based “superheating” gradient applied to the molten phase for a number of hours prior to crystal growth [10, 11]. From the evidence present in literature showing how superheating improves crystal quality in non-layered compounds, the technique was applied for the first time to a layered material by modifying the Bridgman growth of BiI_3 with superheating gradients.

The superheating technique was successful in reducing the concentration of void defects by over an order of magnitude [2]. As was shown in other compounds, a certain temperature

gradient exists that enables enough mass transfer to allow the dispersion of ionic pre-nuclei and improve the quality of the crystal. As shown in the BiI_3 micrographs in Figure 5, superheating gradients of 35 K were optimal for the reduction of void inclusions. In both the edges and bulk of the material, the concentration of voids in samples grown with sufficient superheating gradients were drastically lower than control samples, or samples grown with small gradients. On average, voids concentrations were found to reduce from 4600 voids/cm^3 down to 300 voids/cm^3.

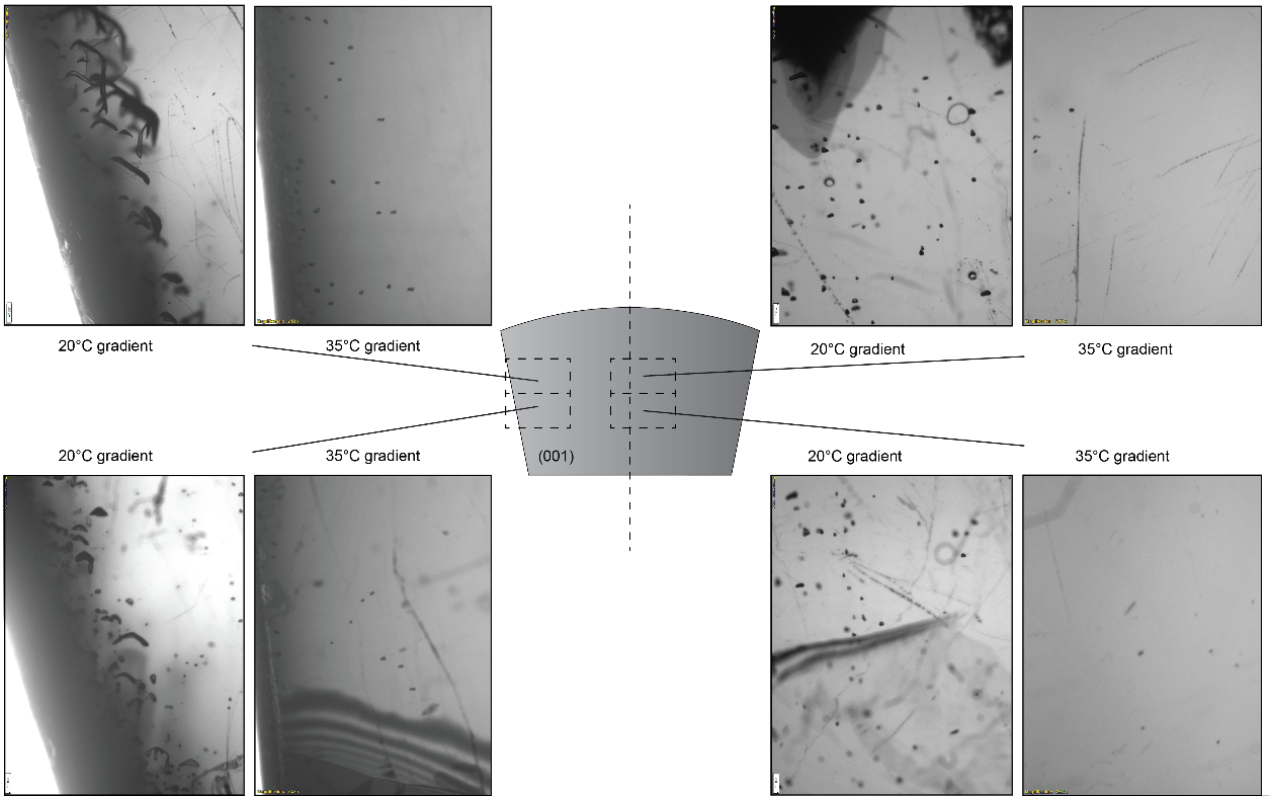

Figure 5. Reduction in void defect density between 25 K and 35 K in BiI_3 crystals grown with a modified Bridgman method including superheating gradients.

The phase quality of superheated Sb:BiI_3 was analyzed through X-ray diffraction rocking curves. Crystals grown without convective superheating as well as those grown with 20 and 35 K superheating gradients were analyzed at the Pacific Northwest National Laboratory's William R. Wiley Environmental Molecular Science Laboratory for ω-scan X-ray diffraction analysis. The findings, presented in Figure 6, show that samples with a 35 K superheating gradient exhibited much higher resolution than those without superheating and with an insufficient degree of superheating. In addition, the samples of Sb:BiI3 grown at 35 K superheating conditions were found to have a 0.0827˚ full-width-half-max (FWHM) rocking curve peak, the most well-resolved peak ever reported for the material.

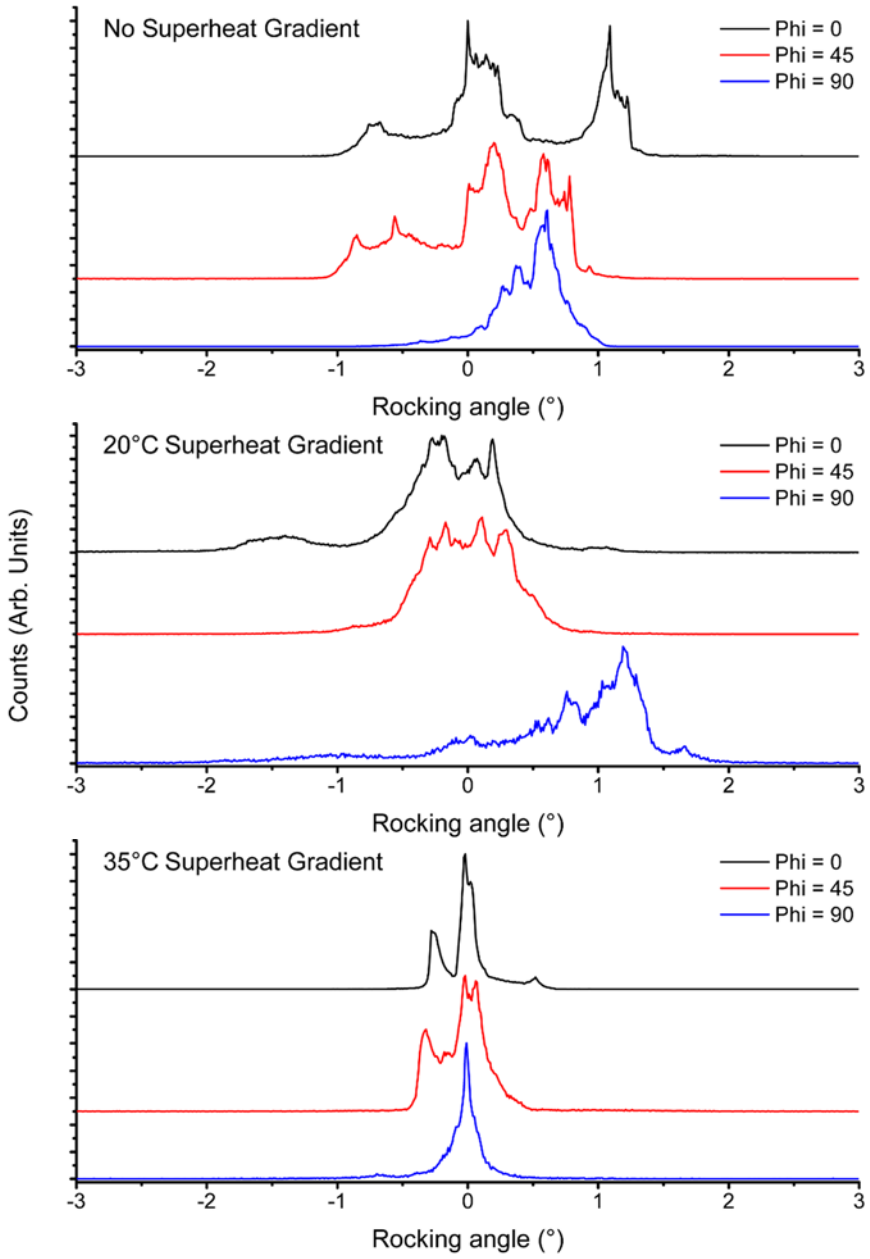

Figure 6. XRD rocking curves on BiI_3 single crystals show non-superheated and insufficiently superheated samples are made up of composites of several superimposed I-Bi-I layers.

Compositional Characterization

For detecting radiation, the precedent set by most cubic-structured semiconductors is that sub-ppm levels of impurities are required in the starting materials in order to produce crystals with the low trap densities necessary for optimal electronic properties. Because impurities can create scattering centers for charge carriers, enable recombination sites where charges are quenched, and negatively impact resistivity and leakage currents, purity is a major requirement in the best

detector materials. It is therefore important to have a strong understanding of impurity concentration within BiI_3 crystals. Compositional characterization has been performed throughout this work through X-ray fluorescence spectroscopy (XRF), inductively coupled plasma atomic emission spectroscopy (ICP-AES), and neutron activation analysis (NAA).

Fortunately, the thermodynamics of crystallization in layered compounds are in favor of preventing impurities from incorporating within the bulk as easily as they are in cubic structures. For instance, in the layered compound InSe, it was found by Chevy that the majority of dopants had no effect on the carrier concentration in doped samples [12]. Segregation coefficients for even isoelectronic dopant/impurity species were well above unity, allowing most impurities to drift to the last-to-freeze region of the crystal. The favorable thermodynamics that limit impurity incorporation is seen in the NAA data presented for BiI_3 in Figure 7. In this study, the composition of thin (> 1 mm) sections taken from the mid-plane and the last-to-freeze portions of a BiI_3 crystal are compared. The crystal analyzed was grown at a rate of 0.5 mm/hr, with no prior refinement performed, and was irradiated for one hour at a $6 \cdot 10^{10}$ n/cm^2-s flux in the University of Florida Training Reactor. The spectra shown in Figure 7 were collected after the irradiation with an HPGe detector over a count time of 30 minutes. This qualitative data shows that the mid-plane of the crystal featured signals denoting the presence of Au and Na impurities in low concentrations, but no others impurity elements at a minimum sensitivity of 10 ng. The top of the crystal, however, showed the presence of Yb, W, Au, Br, and Na trace impurities. The presence of Na in both spectra most likely comes into the crystal via diffusion from the borosilicate glass ampoules used for growth. With the exception of Au, the other impurities present in the crystal all float to the last-to-freeze zone of the crystal boule during the growth process. Overall, the NAA tests on undoped BiI_3 proved that there is a strong segregation of impurities out of crystal bulk during the Bridgman growth process. From the compositional characterization study by NAA, it was concluded that efforts to refine the crystal precursor powders were unnecessary, and even deleterious to the BiI_3 produced in cases where the refinement process depleted the stoichiometry of the crystal boule.

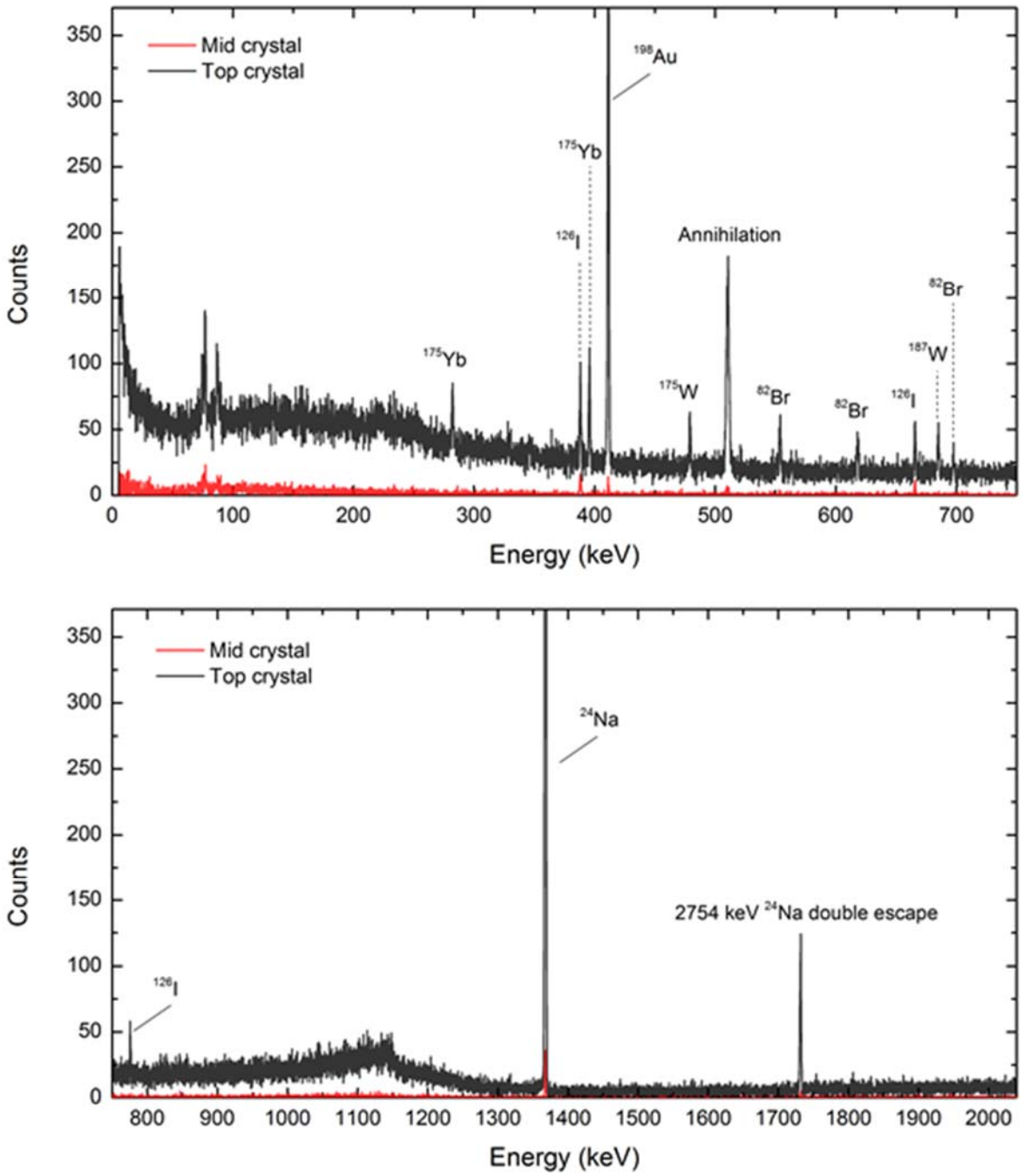

Figure 7. Spectra obtained from the neutron activation analysis (NAA) of BiI_3. A section from the midpoint plane of a single crystal is compared with a section from the top of the boule.

The segregation findings in undoped BiI_3 crystals shed concern on the ability of Sb-doped BiI_3 to retain the Sb dopant in the bulk of the crystal. NAA was performed on a 1000 ppm Sb-doped BiI_3 sliced into thin (< 1 mm) sections. The resulting activation spectra, as shown in Figure 8, were analyzed to determine the segregation of Sb throughout the lattice.

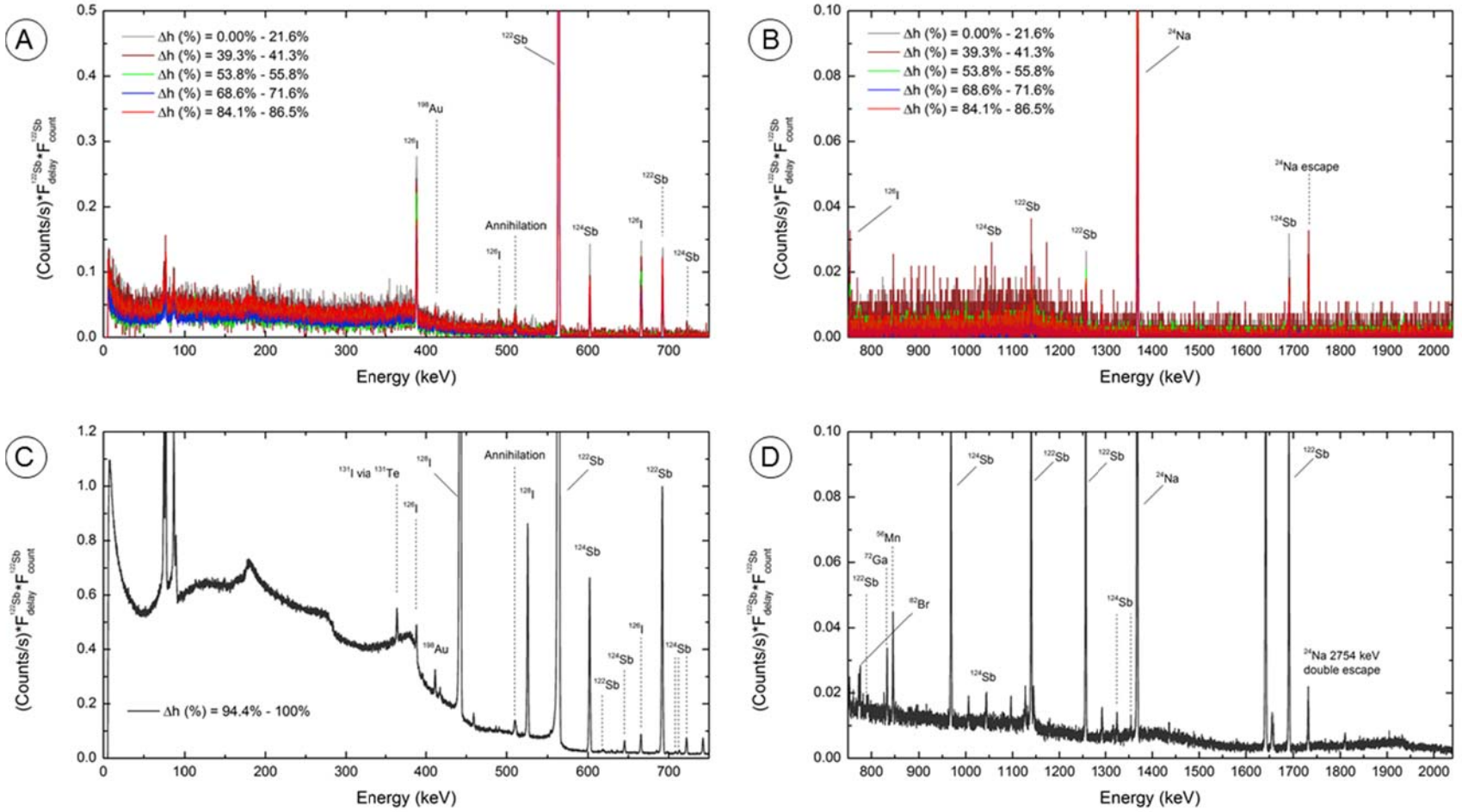

Figure 8. The neutron activation analysis gamma ray spectra on BiI_3 crystals co-doped with Sb and Te. Spectrum (A) and (B) show the low- and high-energy spectra obtained from the bottom of the crystal through 86.5% of the axis. Spectra (C) and (D) show the low- and high-energy spectra from the very top of the crystal. All Spectra are adjusted for mass, as well as correction factors for the time between irradiation and measurement, as well as the duration of the measurement itself.

Spectra from bulk sections harvested from 0 to 94% up the axis of the boule are shown in spectra A and B of Figure 8. In these regions of the crystal, approximately 10% of the Sb doped into the crystal was found to be solubilized into the lattice. The top of the crystal, from 94% to 100% up the crystal axis, contained a drastically higher percentage of Sb. As seen in Figure 8 spectra C and D, the top of the crystal featured higher normalized count rates for Sb, and contained a number of secondary peaks from impurity species. The results of the compositional characterization showing the mass concentration of Sb found in each region of the crystal as well as the segregation coefficient, k_{eff}, is presented in Table 1. The NAA study on Sb-doped BiI_3 gave evidence overall that the Sb dopant exhibits a high degree of segregation in the lattice. With only ~10% of the mass concentration of Sb being retained in the bulk of the crystal, it is necessary to properly adjust the amount of SbI_3 loaded into a BiI_3 charge prior to crystal growth to attain a desired bulk mass concentration.

Table 1. Compositional characterization of 1000 ppm Sb-doped BiI_3.

Axial position range	Δx (cm)	Sb concentration (ppm)	k_{eff}
0.00% - 21.6%	8.978	158.86	0.0562
39.3% - 41.3%	0.852	111.60	0.2650
53.8% - 55.8%	0.804	97.612	0.1750
68.6% - 71.6%	1.247	95.928	0.1100
84.1% - 86.5%	1.003	140.69	0.0077
94.4% - 100%	2.340	1589.3	0.0399

Objective 3: Crystal Cutting, Polishing, and Surface Passivation

The processing methods used to fashion a raw crystal of a compound into a detector are extremely important in determining how it responds to radiation. Each step of the detector fabrication process (ampoule removal, cutting, grinding, polishing, electrode application, passivation, etc.) has the potential to introduce surface or subsurface defects to the crystal. Such imperfections can negatively affect the electronically active volume of a detector, creating various sources of signal noise (shot noise, thermal noise, 1/f noise) which ultimately degrades the gamma-ray detection performance of the sensors [13]. After the surface of a crystal is cut, it is necessary to polish off the surface damage caused by the abrasion between the crystal and the cutting instrument. Rough surfaces create conduction pathways where shunt current can pass

from electrode-to-electrode without going through the bulk, which increases the leakage current of the detector. Additionally, polishing the surfaces of a detector material is necessary to prevent recombination centers formed from the surface defects creating degenerate energy levels. The sum of bulk and surface recombination effects determine the charge collection efficiency and the μτ product of a semiconductor crystal. The surface contribution term is not negligible when it comes to detector performance [14]. In fact, it is seen in many prominent detector materials (CZT, HgI_2, TlBr, etc.) that the surfaces perpendicular to the electroded surface of a crystal are likely to host recombination centers and feature excess leakage current due to the damage induced by the cutting process [3, 15, 16]. The smoothest surfaces therefore produce the lowest leakage currents in detectors.

Fortunately for BiI_3, if a crystal has been properly orientated prior to cutting, then only the (100) and (010) oriented surfaces need to be polished, as the (001) surface can be prepared through cleaving with adhesive tape. Use of a lubricant is necessary during cutting and polishing of the BiI_3 crystal surface to reduce friction-induced heating and prevent excess damage to the surface. Heavy mineral oil was used as lubricant in this work, and it was dissolved from the samples after cutting and polishing using cyclohexane. The cutting of BiI_3 spectrometer crystals performed in this work was performed exclusively with a diamond-embedded endless wire saw (STX-201, MTI Corporation) featuring a 300 μm diameter wire. A rotational speed of 90 rpm was maintained when cutting all BiI_3 surfaces. Due to the softness of these crystals, the speed of the cut through the crystal was controlled by-hand, to allow a cutting rate of approximately 1 mm per minute. Following cutting, BiI_3 crystals examined in this work were polished incrementally with SiC-embedded polishing pads from 300 grit, 600 grit, and 1200 grit. The crystals were then manually polished to a highly reflective finish using 1 μm and then 0.05 μm Al_2O_3 powder dispersed in heavy mineral oil. A series of micrographs showing the polished surfaces of a BiI_3 crystal at various finishes are shown in Figure 9. Finally, the remaining oil on the BiI_3 crystals was removed by sonicating the crystals in a beaker of cyclohexane. Cyclohexane is a nonpolar solvent that dissolves oil without reacting with the BiI_3.

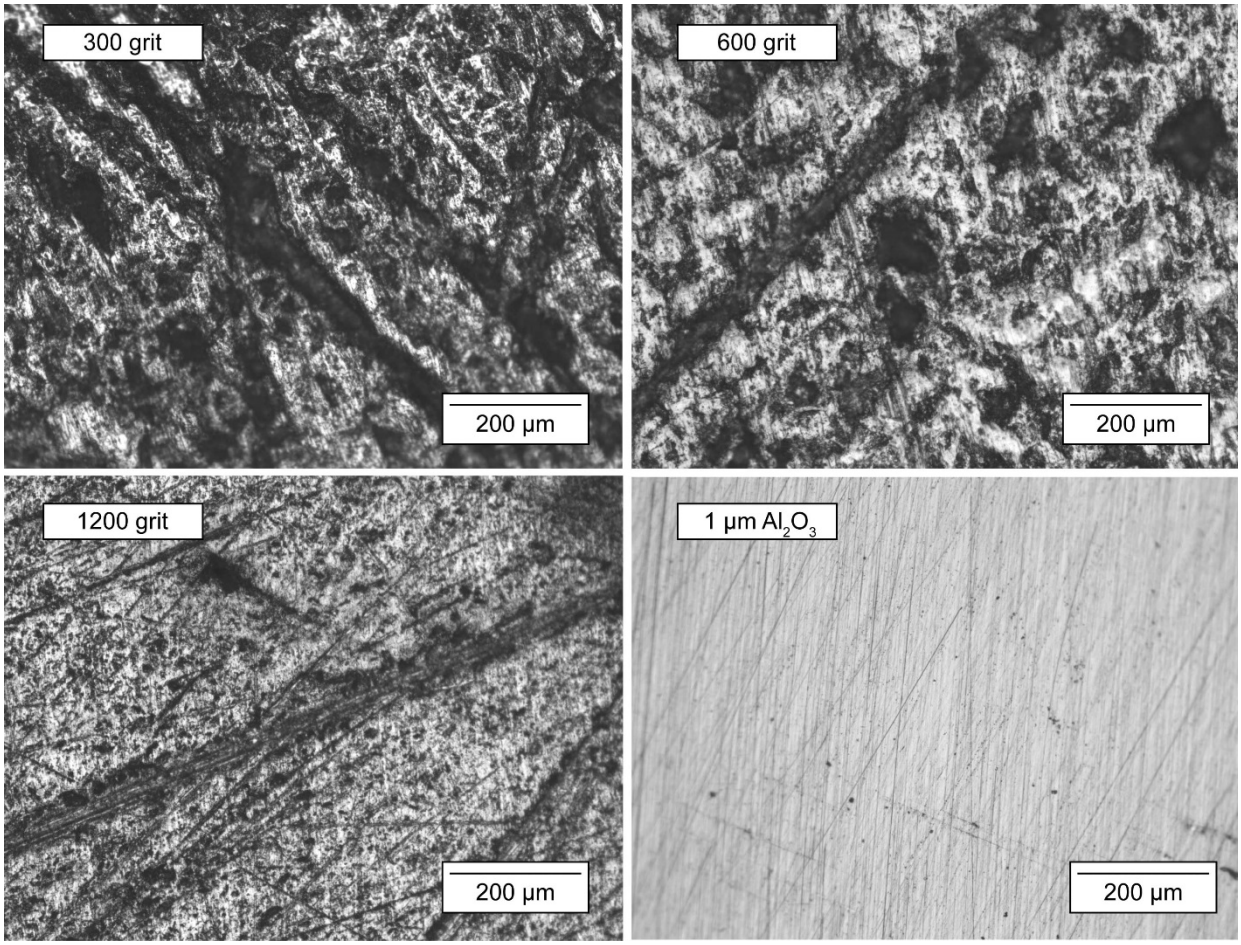

Figure 9. Micrographs of the BiI_3 (010)/(100) surface after polishing to various surface finishes.

Even after polishing, it is inevitable that some surface damage will be present on the sides of the crystal due to mechanical ablation. To remove this damage from the surface, the chemical polishing of RTSD crystals is often performed following mechanical polishing. Notably, BiI_3 gamma ray detectors have exhibited improvements to surface morphology and detection performance following the application of chemical etching [17]. Because BiI_3 is highly reactive, a solvent that removes surface damage without forming negative chemical species is desired. Solvent solutions of 10% KI and methanol, pure methanol, ethanol, isopropyl alcohol (IPA), and acetone have been examined for their suitability as a surface etchant. To examine different types of processing a “light etch”, where the solvent was swiped on the sides of the crystal with a damp cotton swab (50 swipes/side), and a “heavy etch” where the entire crystal was soaked in the solvent for 30 seconds, were examined for several samples. The effects of both light etching and heavy etching for different solvents are shown in Figure 10. For the light etching process, the side surfaces retained their mirror finish in every case except the 10% KI/methanol solution. Methanol,

IPA, and acetone had a positive impact on increasing the resistivity of the crystals, while the other solvents examined led to lowered resistivity. The data presented in Figure 10 suggests that a shunt current is present in BiI_3 samples not treated with chemical etchants. However, the different trends seen between solvents shows that the surface leakage, which is influenced by factors such as "dangling" bonds, are influenced strongly by the solvent used to perform the etching. Optimization of solvent species and BiI_3 etching procedure should be the subject of future studies.

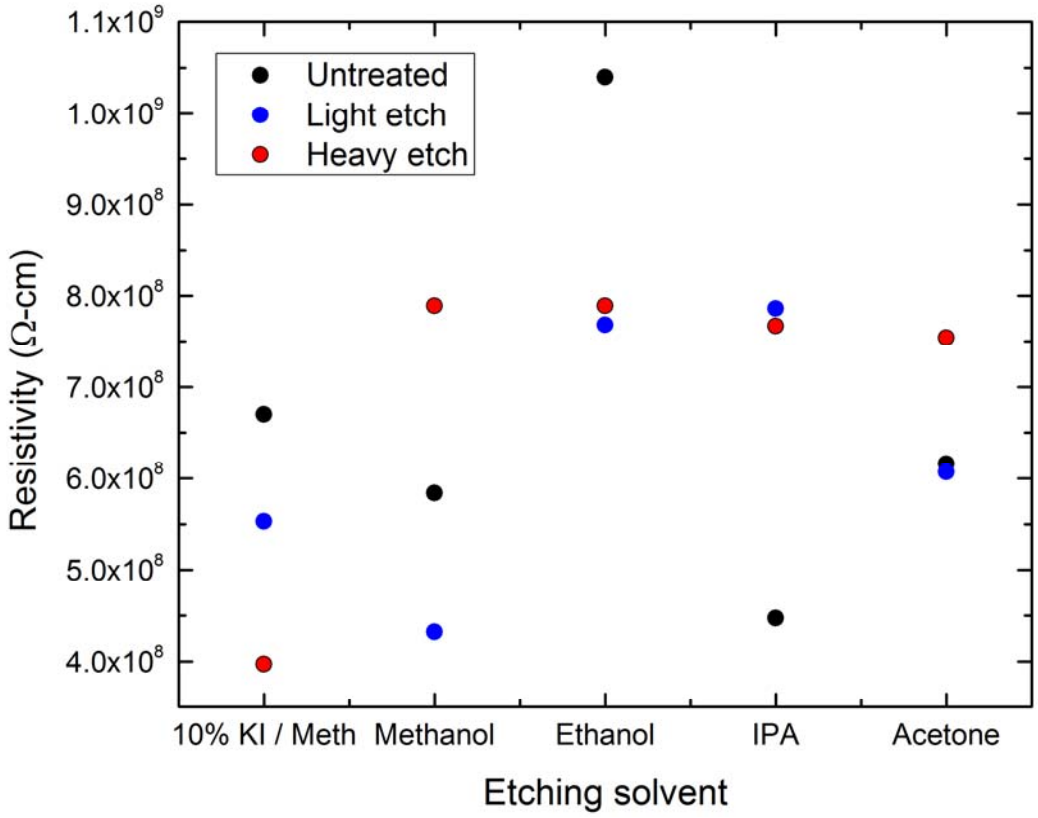

Figure 10. The effect of chemical etching on the resistivity of BiI_3 crystals using different solvents and etching techniques.

An image of a BiI_3 crystal that has been cut, polished, and rinsed with cyclohexane is presented in Figure 11. At this point in the detector processing, the crystal is ready to be electroded with a metallic contact. In this work, Au was primarily used as the electrode material for creating Ohmic current-voltage behavior. To prepare the (001) surface for electrode deposition, cleaving to a smooth finish must be performed to prevent discharges from high bias along (001) structures during detector operation. The process of cleaving is as simple as taking adhesive tape, applying it flat onto the entire (001) surface, and removing planes of I-Bi-I until the surface is optically smooth. It may take several dozen cleaves in order to finally produce a (001)

plane that is smooth enough for electrode deposition. Over the course of this work, many different tapes were used for cleaving; however, black 3M ® electrical tape featured the best degree of adhesiveness for allowing the planes to be cleaved off efficiently.

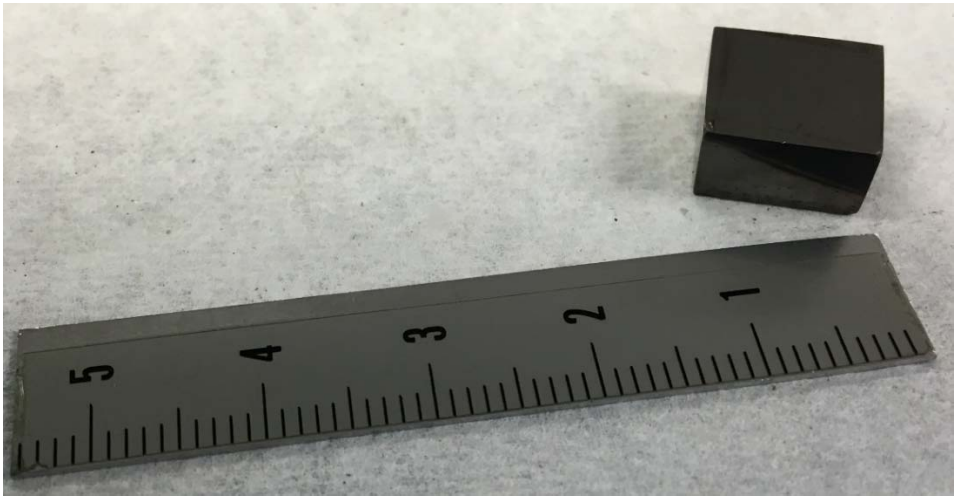

Figure 11. A 0.84 cm^3 Sb:BiI_3 single crystal analyzed in this work. Units of scale in the image are cm.

Following chemical polishing, a protective surface passivation layer is applied crystals of BiI_3 fashioned for spectrometers. This passivation layer prevents effects from oxidation, which include the formation of BiOI surface layers that degrade electronic properties. Early in this work, Parylene-N was coated onto the crystals using a Parylene sputtering chamber. It was found, however, that the Parylene deposition process was mechanically damaging the BiI_3 crystals due to their softness and plasticity. The RTSD compound TlBr suffers from similar problems, so the techniques used to passivate TlBr were applied to BiI_3 to support passivation. The passivation method developed for BiI_3 involves using commercially available epoxy to cap the BiI_3 crystals after they are electrically connected to their IC substrates. This simple processing step has been shown to help prevent the offset of Ohmic behavior from oxidation effects following extended periods of high bias in BiI_3 detectors.

Objective 4: Electrode Deposition and Electrical Property Measurement

Electrode selection is very important to obtaining the desired Ohmic performance of RTSD devices. Ohmic behavior is exhibited when the leakage current of a semiconductor increases or decreases linearly with the applied voltage. For an Ohmic junction to form, at a metal-semiconductor interface the work function of the metal should be lower than that of the semiconductor such that there is no potential barrier blocking current flow. Additional phenomena

that take place at the interface between a semiconductor and a metal electrode, such as Schottky emission, thermal tunneling, or Fowler-Nordheim (quantum) tunneling, can limit the resistivity of the detector [18]. BiI_3 crystals on average exhibit greater resistivity when electroded with Pt contacts. However, it has been shown by Qiu *et al.* that Pt is not a chemically optimal electrode material due to its tendency to initiate decomposition that separates Bi, Pt, and I into metallic layers [19]. Thus, throughout this work, the metal Au has been used as the electrode material due to its superior compatibility with the surface chemistry of the BiI_3 (001) plane.

A summary of the electronic properties of BiI_3 are provided in Table 2. In general, while vapor transport growth enables BiI_3 to be grown with better stoichiometry and exhibit superior electronic properties, the yield and growth rate are much poorer than melt-growth based techniques. In this work, better leakage current and resistivity values from BiI_3 crystals have been reported than previous investigation of the material. The enhancement to electronic properties comes from the superior processing methods applied in this work. Additionally, for the first time, mobility values for holes have been reported. The hole mobility, as previously reported, is a number of magnitudes worse than electron mobility. This finding highlights the necessity of single polarity charge sensing techniques when measuring radiation spectra with BiI_3.

Table 2. Reported property values for BiI_3 synthesized from melt-growth based techniques as well as vapor transport (VT) techniques

	Crystals		
	Melt	VT	References
Resistivity (Ω-cm)	$5 \cdot 10^8$ - $2 \cdot 10^{10}$	$1.6 \cdot 10^{11}$	[20, 21], this work
Leakage current ($\mu A/cm^2$)	$\sim 10^2$	$\sim 10^{-1}$	[22], this work
Band gap (eV)	1.67 ± 0.09		[23]
μ_e (cm^2/Vs)	600 ± 50	433 ± 79	[22, 24, 25]
μ_h (cm^2/Vs)	0.01	--	This work
$(\mu\tau)_e$ (cm^2/V)	$\sim 10^{-4}$		[26, 27], this work
Pair creation energy (eV)	5.8		[21]
Dielectric constant	8.6 ($E_{\parallel}$ c-axis)		[28]

Throughout this work, nearly every crystal of BiI_3 processed for becoming a radiation detector had its current-voltage properties analyzed. Figure 12 shows the current density plotted against electric field for a number of BiI_3 samples, along with the average resistivity extracted from the data for each electrode metal.

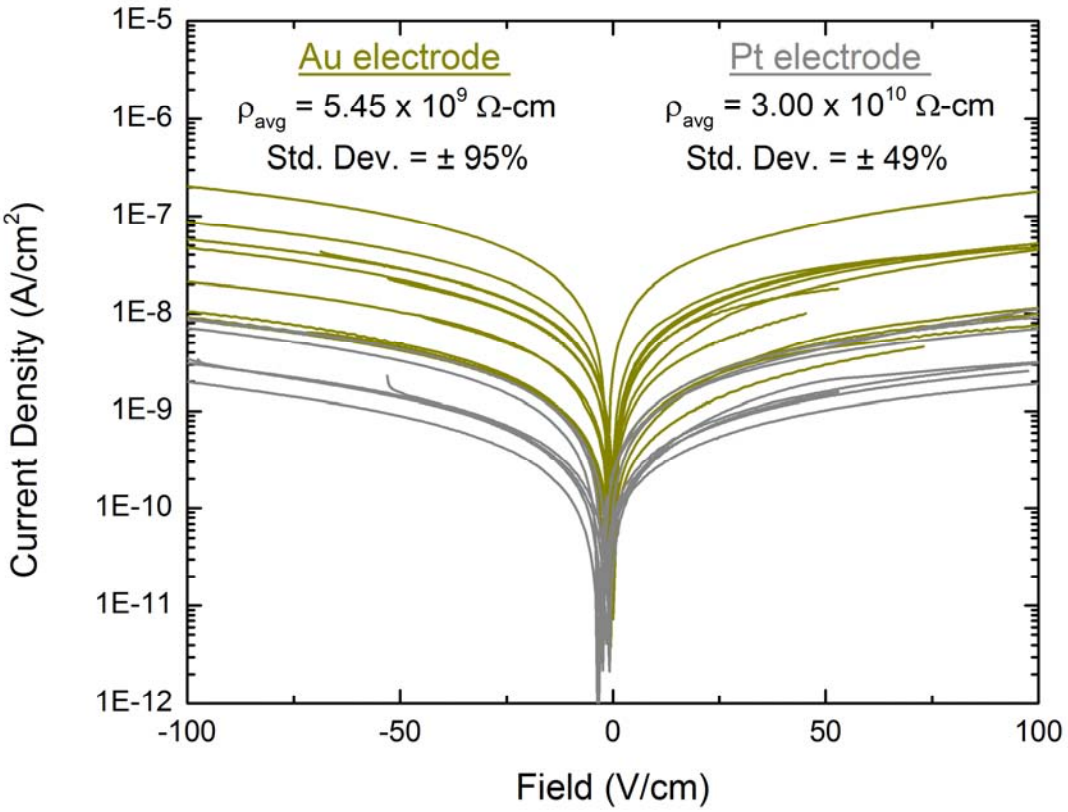

Figure 12. Current-voltage behavior for a number of BiI_3 crystal electroded with Au or Pt electrodes.

Resistance from grain-to-grain charge hopping destroys the capability for charge to be induced effectively on an electrode from a single radiation interaction. Extremely high resistivity in bulk single crystals of BiI_3 is actually a cause for concern, as it can indicate macroscopic separation between (001) planes and imply that leakage current is affected by a physical gap in the sample rather than the band structure of the material. Figure 13 presents an example of this, where a sample that exhibited resistivity of nearly 10^{13} Ω-cm does so due to plane delamination. Care should always be taken to examine bulk BiI_3 samples visually and through microscopy to determine that no signs of macroscopic plane delamination are present.

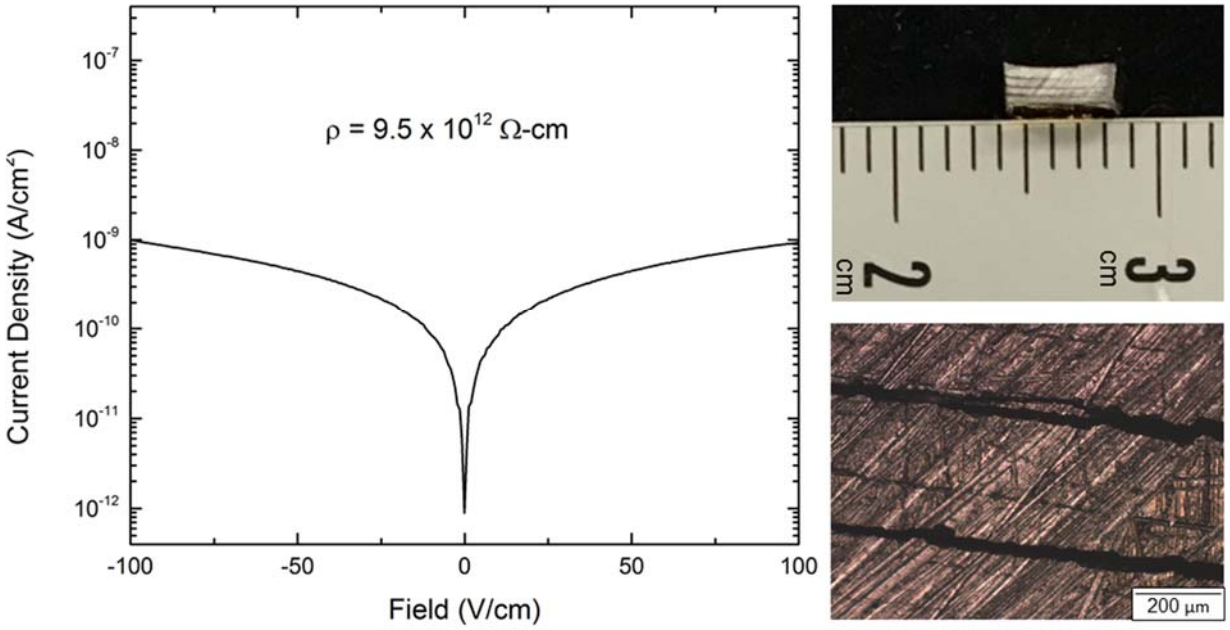

Figure 13. Artificially high resistivity in a layered BiI_3 crystal can often come about as a result of physical separation between (001) planes, as shown by this comparison of I-V plots and micrographs.

It was discovered through the course of this work that BiI_3 undergoes the transient current peak phenomena reported by Levi *et al.* for HgI_2 [29]. A current transient peak can be observed when a voltage reversal is performed shortly before performing a leakage current measurement, and arises due to the slow de-trapping of holes as they drift to the cathode. The time at which the transient occurs, as well as its magnitude, are a function of the applied bias after the polarity reversal. Examples of this phenomena are seen in the works of Han *et al.* [25] and Gokhale *et al.* [17] as well as this work. This effect has implications in the acquisition of gamma ray spectra, as drifting space charge created by the de-trapping holes can interfere with charge induction from the electrons generated in gamma-ray interactions. These transient currents make it impossible to see proper signals from radiation upon initially applying a bias. Because of this, BiI_3 must be given sufficient time (several minutes) to achieve thermal equilibrium and allow the transient currents to resolve before spectra can be acquired. The trap-controlled mobility, which can be derived from the current transient peak, will be the subject of future studies on BiI_3.

Lintereur *et al.* and Gokhale *et al.* examined high purity BiI_3, and reported μ_e values of 433 ± 79 cm^2/Vs for PVT synthesis powder, 260 ± 50 cm^2/Vs for melt-grown crystals, and no detectable mobility signal from holes [30]. Incorporating the Sb dopant into BiI_3 crystals has been reported to improve mobility. In the work by Han *et al.* examining Sb-doped BiI_3, electron mobility

in excess of 1000 cm^2/Vs was reported in some samples [25]. Mobility, μ, is measured for electrons by irradiating the cathode and determining the rise time on the leading edge of the pulse output by a preamplifier. Then, taking into account detector thickness, D, and the applied electric field, E, the relation

$$\mu = \frac{D}{t_{rise} E} \tag{1}$$

is used to calculate the mobility. An example of this method applied to a 1000 ppm Sb-doped BiI_3 crystal is shown in Figure 14. Throughout this work, the mobility and values for Sb:BiI_3 have remained constant with the values reported in the works by Gokhale and Han [25, 31].

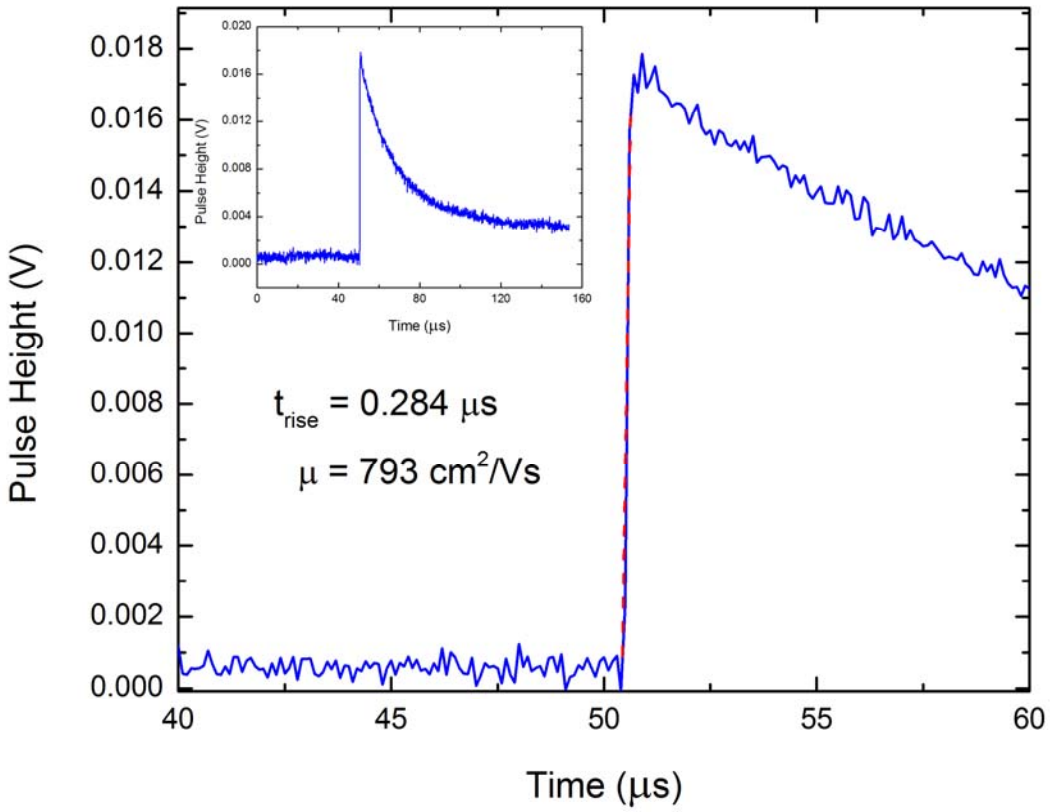

Figure 14. The preamp output and rise time from a ^{137}Cs signal in a Sb:BiI_3 detector. Mobility is extracted from the rise time of the leading edge on the preamp output pulse (red dashed line).

The first published ($\mu\tau$) value for charge carriers in BiI_3 was reported by Dmitriyev as $9.5 \cdot 10^{-6}$ cm^2/V for electrons, and undetectable (below 10^{-7} cm^2/V) for holes [20]. Recent studies on charge collection efficiency using this value of ($\mu\tau$) have shown unachievable values of electric field are needed (100,000 – 2,000,000 V/cm) in order to achieve reasonable charge collection efficiency [32]. In this work, BiI_3 has demonstrated $(\mu\tau)_e$ values on the order of 10^{-4} cm^2/V-s.

Objective 5: Electrode Geometry Optimization

Controlling the weighing field and weighing potential experienced by charge carriers is very important to improving the spectral resolution of BiI_3 detectors. Parallel plate electrode geometries are simple to manufacture and work well when performing simple electrical characterization on crystals. However, the equal importance given to electrons and holes in parallel plate geometry are detrimental to obtaining spectra from gamma rays. Throughout the entirety of this work, a well-resolved gamma ray spectrum has never been obtained from a BiI_3 crystal without the use of designing the electrode geometry to allow the bulk of the charge from ionization to be induced on the anode alone.

Because the induced charge on the collecting electrode is determined by the movement of both charged species, signal resolution becomes worse based on the difference in the ability of the two carriers to induce charge at the electrode. An illustration of this phenomenon is shown in Figure 15. In the case of the perfect semiconductor, the induced charge on the electrode is equal to the total charge generated, while in the realistic case the induced charge is much less than the total due to incomplete collection of the minority carrier.

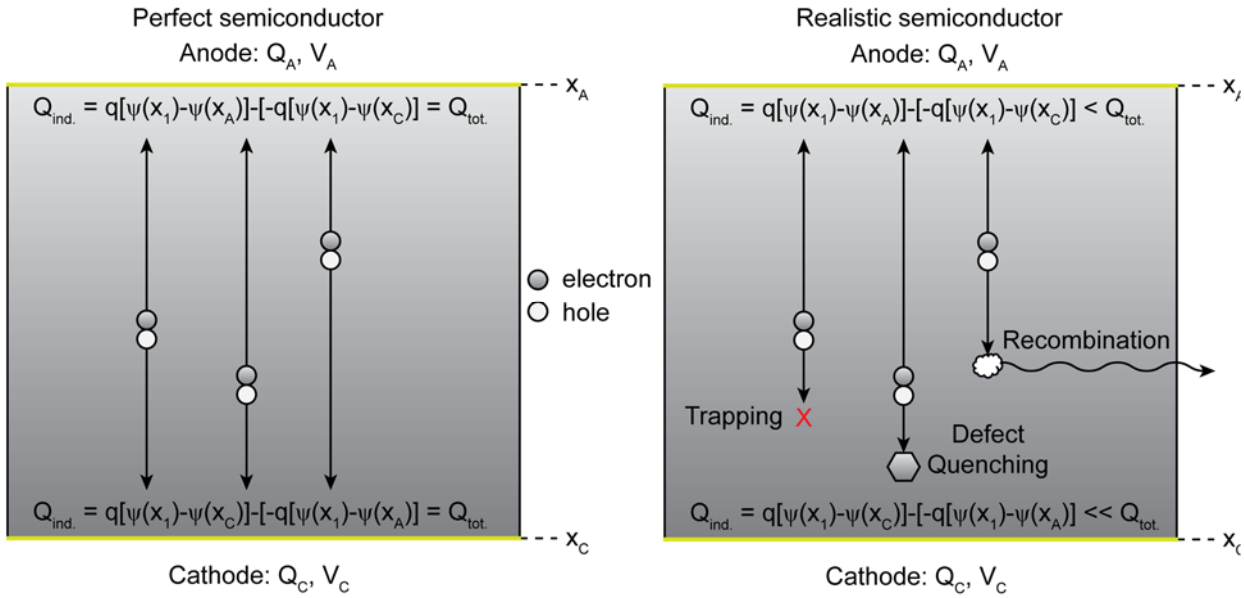

Figure 15. As electrons and holes transit throughout a semiconductor, they induce charge on the collecting electrode proportional to the difference in weighing potential between the site of their generation and the site of their termination

Most RTSD candidates feature a majority and minority carrier, where either the electrons or the holes have significantly better transport properties through the crystal lattice. For instance, due to the severe carrier trapping shown in layered iodide compounds [17, 19] including BiI_3 [25],

electrons are much more mobile than holes. After a gamma ray interaction occurs, free electrons will begin to drift toward the anode where they will induce a negative charge until they are collected. In a likewise manner holes will move toward the cathode; however, the movement of the positively charged holes away from the positively charged anode will induce a net negative charge on the anode as well. Because induced charge is proportional to $\Delta\psi$, it is therefore possible to create weighing potential distributions where nearly all of the induced charge is due to the majority carrier. Using the finite element analysis software Agros2D [33], a number of electrode configurations were built to show the effect that electrode geometry has on weighing potential. In each model, a BiI_3 crystal with 1 cm width and 1 cm height was constructed with a 1000 V bias applied to the cathode. A semiconductor electroded in a parallel plate geometry as depicted in Figure 16.

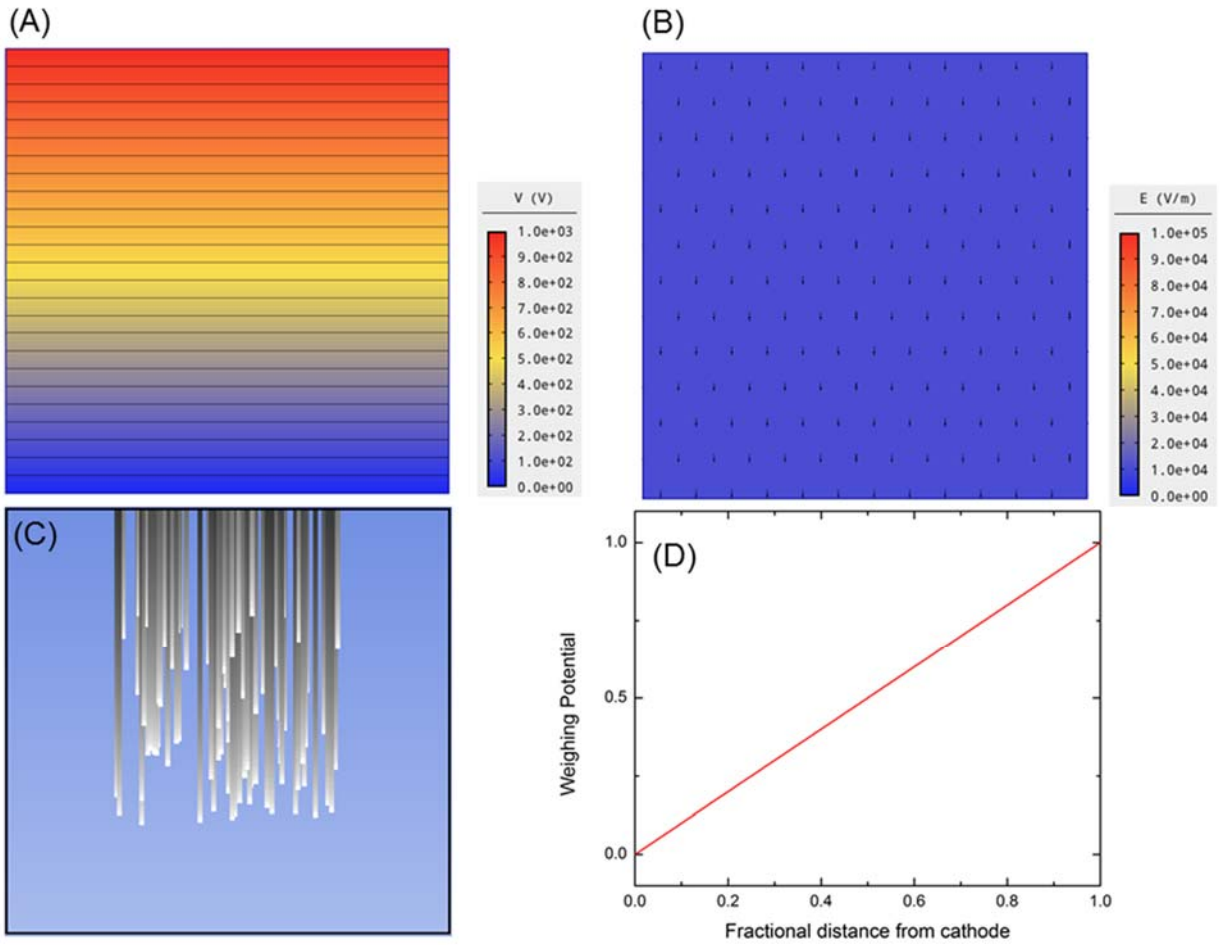

Figure 16. (A) Electric field and (B) scalar potential profiles for a 1000 V bias across a 2D construction of a 1 cm^3 BiI_3 crystal with a parallel plate geometry. (C) Shows a simulation of the particle tracks of 100 electrons generated in the bulk of the crystal. (D) presents the weighing potential as a function of depth along the centerline of the crystal

In a parallel plate electrode geometry, every electric field line vector begins at the cathode and ends at the anode. The electric field across the crystal is a constant 1000 V/cm at every position due to the bias applied to the cathode. Therefore, from Figure 16, the scalar potential and weighing potential in this crystal follows a linear distribution. The weighing potential on a negative charge dropped at some position *x* within a planar-contacted semiconductor will therefore induce a charge on the anode proportional to $\psi(x)-\psi(x_{anode})$. If electrons are generated at position 0.9x, where x is the distance from the cathode to the anode, they will induce only 10% of the total induced charge while the drift of the hole will generate the other 90%. If the hole undergoes some sort of impeding effect, the remainder of charge is lost. Charge collection efficiency in a parallel plate geometry is derived from the Hecht equation as

$$CCE(x) = \frac{V(x)}{L}\left[(\mu\tau)_e\left(1-\exp\left[\frac{x}{E(x)(\mu\tau)_e}\right]\right)\right] + (\mu\tau)_h\left(1-\exp\left[\frac{x}{E(x)(\mu\tau)_h}\right]\right) \quad (2)$$

.

From Equation (2, in a situation where hole transport is drastically hindered and the induced charge depends only on the electron movement, it can be inferred that the resolution of a photopeak can degrade by up to 200%.

Many of the electrode geometry designs used to remedy induced charge problems collection were adapted from existing gas detector technologies. One such design, pixel electrode grids, enables the low mobility carrier to have less of a negative influence on the resolution output from a semiconductor detector [34]. If a cathode-electrode geometry is devised where the collecting electrode of the minority charge carrier is made much smaller relative to the size of the minority carrier electrode, electric field lines will buckle inward. This curvature of E_W will create a very high weighing potential in the vicinity of the pixel used to collect the majority carrier, yet the weighing potential in the remainder of the crystal will remain low. In this configuration, $\Delta\psi$ for the majority carrier will be very high whereas $\Delta\psi$ for the minority carrier will be very low. Figure 17 presents the scalar potential and electric field distributions for a case where a 1 cm cathode and 1 mm anode are present on a crystal. As shown in plot (D), the minimum amount of induced charge, Q_A/Q_0, in a representative pixel anode is 86% if the charge carrier is generated at the cathode. In contrast, the minimum in a planar geometry could be 0% if severe trapping is present.

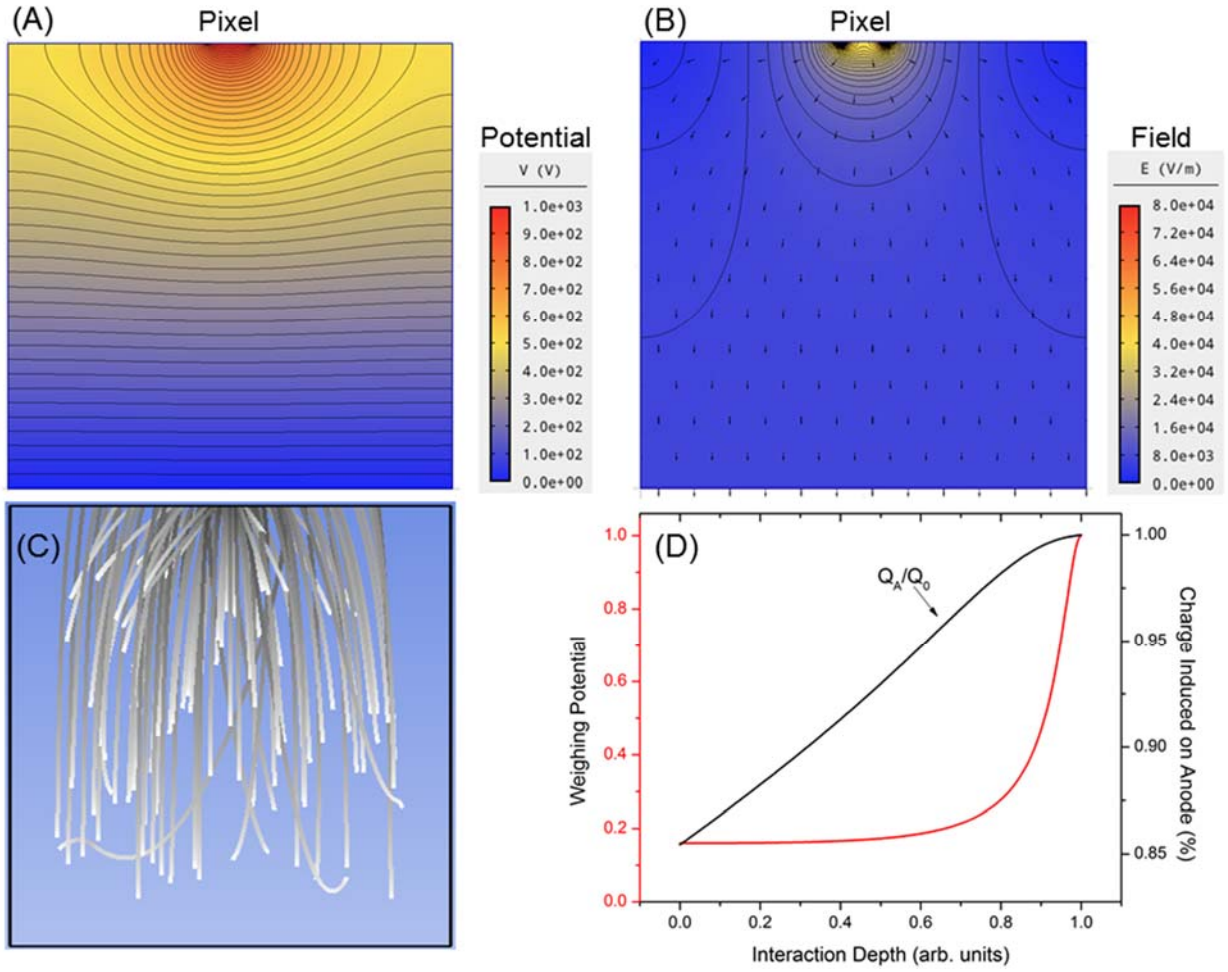

Figure 17. (A) Electric field and (B) scalar potential profiles for a 1000 V bias across a 2D construction of a 1 cm^3 BiI_3 crystal with a coplanar grid consisting of a 1 mm thick pixel as the anode. (C) Shows electron tracks from random generated locations in the crystal, and (D) presents the weighing potential and induced charge ratio.

An example of the importance in controlling the weighing field and weighing potential across an RTSD crystal is shown through Figure 18. Both spectra on the plot were recorded from the same crystal, bias conditions, and ^{137}Cs source over the collection time of 5 minutes. The crystal's (001) pixelated anode surface was cleaved in between measurements and a planar electrode was deposited on the surface instead. The difference between spectral qualities in the two cases is pronounced, as the planar electrode barely exhibited evidence of a photopeak from the 662 keV gamma ray. The pixelated anode however was able to clearly resolve spectral features characteristic of radiation interactions. The detrimental impact of hole trapping, which leads to incomplete charge induction, makes the use of weighing potential modifications a necessity in BiI_3 spectrometers.

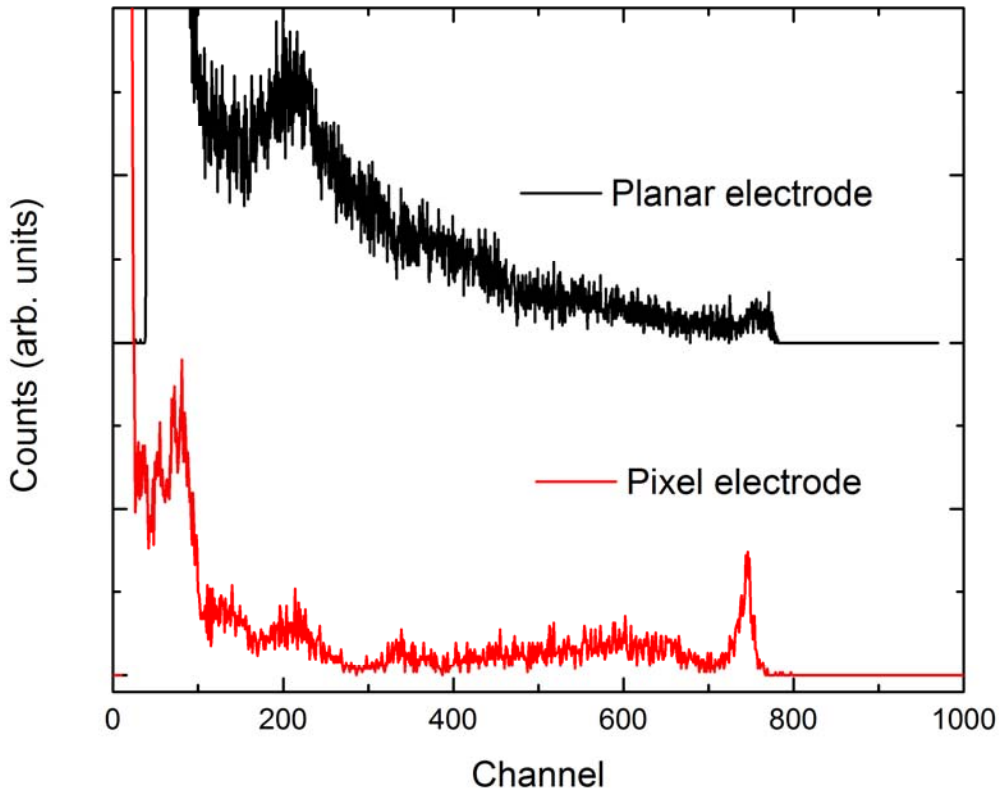

Figure 18. Comparison of signal from a ^{137}Cs source between a BiI_3 sample that featured planar and pixelated electrode geometries. Spectra were adjusted for gain to align photopeak channels.

Utilizing a pixelated grid for the anode of a detector allows the weighing potential to be controlled such that the majority of charge induced in radiation interactions comes from electrons alone, regardless of where in the crystal the interaction occurred [35-37]. The BiI_3 spectrometers fabricated in this work were masked with a 3 x 3 grid of 1 mm^2 pixels. The pixel grid was applied by using a Mo mask to cover the region on the (001) surface of the crystal where the mask was desired to be deposited. The sides of the samples were covered with low-outgassing Kapton tape such that electrode metal was only deposited on one surface of the crystal at a time. Using a Ted Pella Inc. model 108 sputter coater, Au was deposited onto the surface through a magnetron sputtering process. A sample of a BiI_3 spectrometer following the electrode deposition process is shown in Figure 19. Following the electrode application, the Kapton tape was removed from the samples, and the (010) and (100) surfaces were thoroughly swiped with cyclohexane on cotton Q-tips to remove any residual gold that may have permeated through the tape during deposition.

Figure 19. BiI_3 crystal with a 3 x 3 pixel electrode grid following Au electrode deposition.

Objective 6: Detector Electronics Fabrication and Prototype Assembly

After electrode deposition, the crystals are suitable to operate as detectors. In literature as well as this work, BiI_3 has been integrated into detector electronics through two methods. The first method, which has successfully produced signals in a number of works [22, 25, 26, 31], consists of using a conductive “pogo pin” to physically contact the collecting electrode of the crystal with the input capacitor to the shaping electronics. The benefit from this method is its simplicity, as it allows the ability to quickly change out samples and switch collecting pixels. However, many downsides to the pogo pin make it a non-optimal way to collect charge generated in BiI_3 crystals. The spring in the pogo pin is very vibration sensitive, and if oscillated it will produce spurious charges that create noise and false signals. Damage from the physical contact on the brittle surface of BiI_3 can fracture the surface and wear off electrodes in some cases as well. Additionally, a large amount of contact resistance is encountered between the pogo pin and the electrode, which often requires increasing the gain beyond 100x on the shaping amplifier in order to shape the low voltage amplitude output of the preamplifier into a spectrum. However, the most performance-limiting aspect of pogo-pin connections comes from the difficulty of grounding the pixels not being used to sense charge. When the guard ring and non-charge sensing pixels are not electrically grounded, the amount of charge induced onto the sensing anode pixel is greatly diminished; thus, as a result, the efficiency of the detector degrades. This occurs because a significant amount of charge induction is lost when interactions occur outside the volume beneath

the collecting pixel. This phenomenon is shown by the spectra presented in Figure 20. When the guard ring and pixels are not grounded, as is the case in the pogo pin samples, detectors that are biased to equivalent fields and irradiated with the same source exhibit lower efficiency than detectors that have grounded non-sensing pixels. In future work, processing techniques should be applied to BiI_3 to enhance surface resistivity to further improve electric field distribution throughout the detector. As has been shown for CZT, even small levels of surface conductivity can negatively influence the charge collection efficiency of a detector [310].

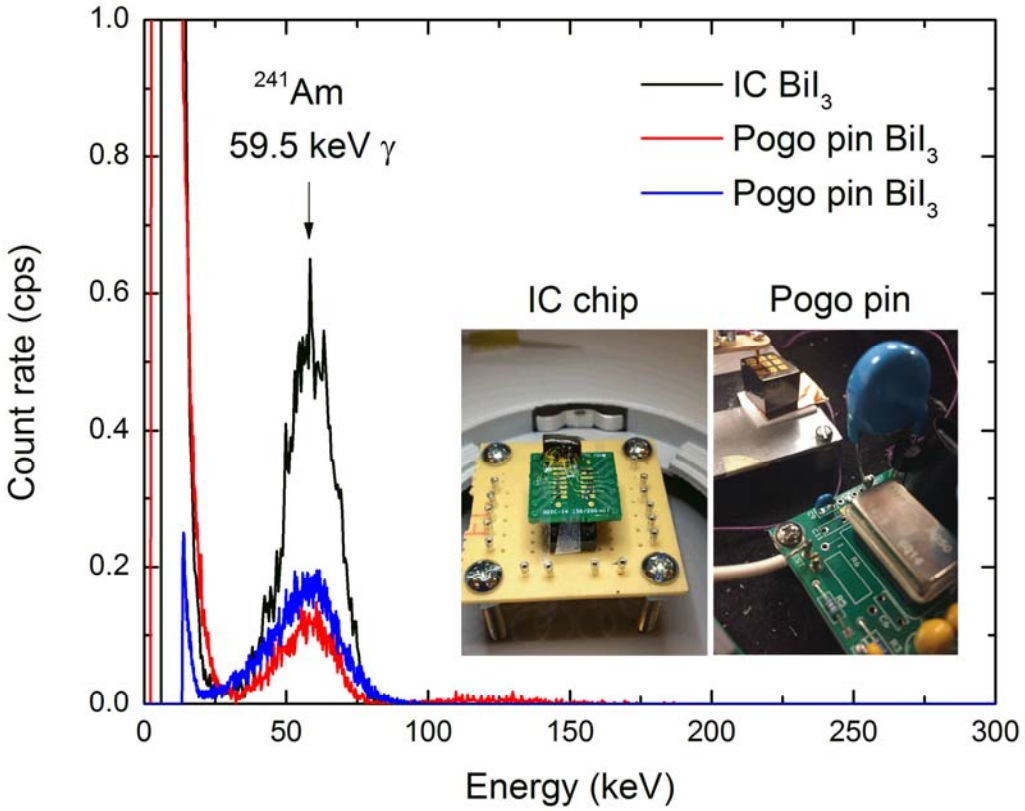

Figure 20. Signals obtained from the 59.5 keV gamma ray of ^{241}Am by BiI_3 detectors fabricated on IC chips (black) and two different samples fabricated with a pogo pin connection (red and blue).

A more sophisticated way of integrating BiI_3 spectrometers into the detector electronics, developed in this work, is through using a conductive paste to bind individual wires to electrode pixels, and utilize an integrated circuit (IC) substrate to supply signals into the preamplifier. Integrating BiI_3 crystals into ICs for signal readout allows for connection into the shaping circuit to be performed with lower contact resistance, allows non-sensing pixels and guard rings to be grounded, and additionally allows multiple pixels to be simultaneously readout to perform depth correction measurements. Figure 21 shows a BiI_3 crystal before and after its assembly onto an IC substrate. The process used in this work involved bonding 0.05 mm Au wires onto individual

anode pixels, guard rings, and cathode with graphite-based conductive paste (Pelco conductive carbon glue, Ted Pella, Inc.). Wires were then bonded to terminals on an SOIC-type chip. Double-sided tape, as seen in Figure 21, was laid down on the SOIC board in order to hold the wires in place so they could easily be bonded to the terminals with conductive carbon paste as well. Following the bonding process, epoxy was used to cap the BiI_3 crystal and IC leads in order to prevent the wires from disconnecting from either the crystal or the board. The capping process plays a role in preventing the breakdown of Ohmic behavior in samples following extended periods of bias. After soldering pins onto the bottom of the SOIC boards, the BiI_3 detectors were integrated into the shaping circuit.

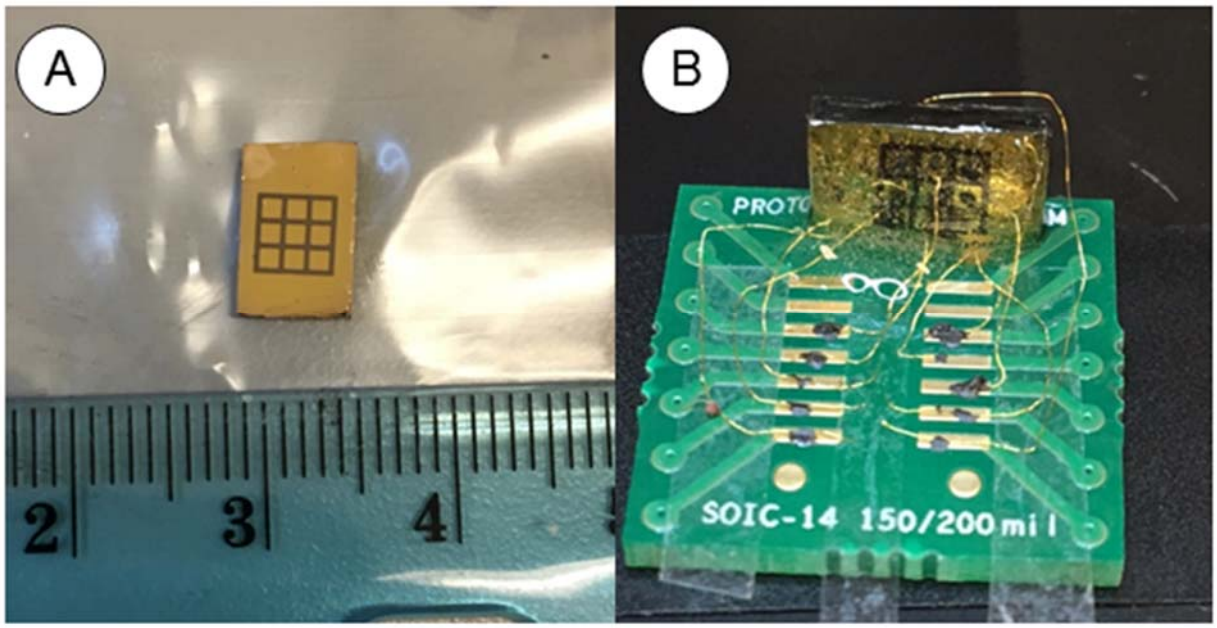

Figure 21. A pixelated BiI_3 sample before (A) and after (B) integration into an IC substrate and capped in epoxy.

In addition to developing processing methods to connect BiI_3 crystals to IC substrates, an electronics test box to enable depth correction was developed to support this work. The depth correction test box is shown in Figure 22. The electronics assembly consists of five Amptek A250 preamplifiers that are used to shape the signals coming out of individual pixels in order to determine the depth within the crystal where gamma ray interaction occurred. In practice, three preamplifiers read out signals from three individual pixel anodes, one preamplifier reads signals from the guard ring, and the last preamplifier reads out signals from the cathode. By measuring the anode-to-cathode signal intensity ratio the depth within the crystal in an individual interaction can be determined.

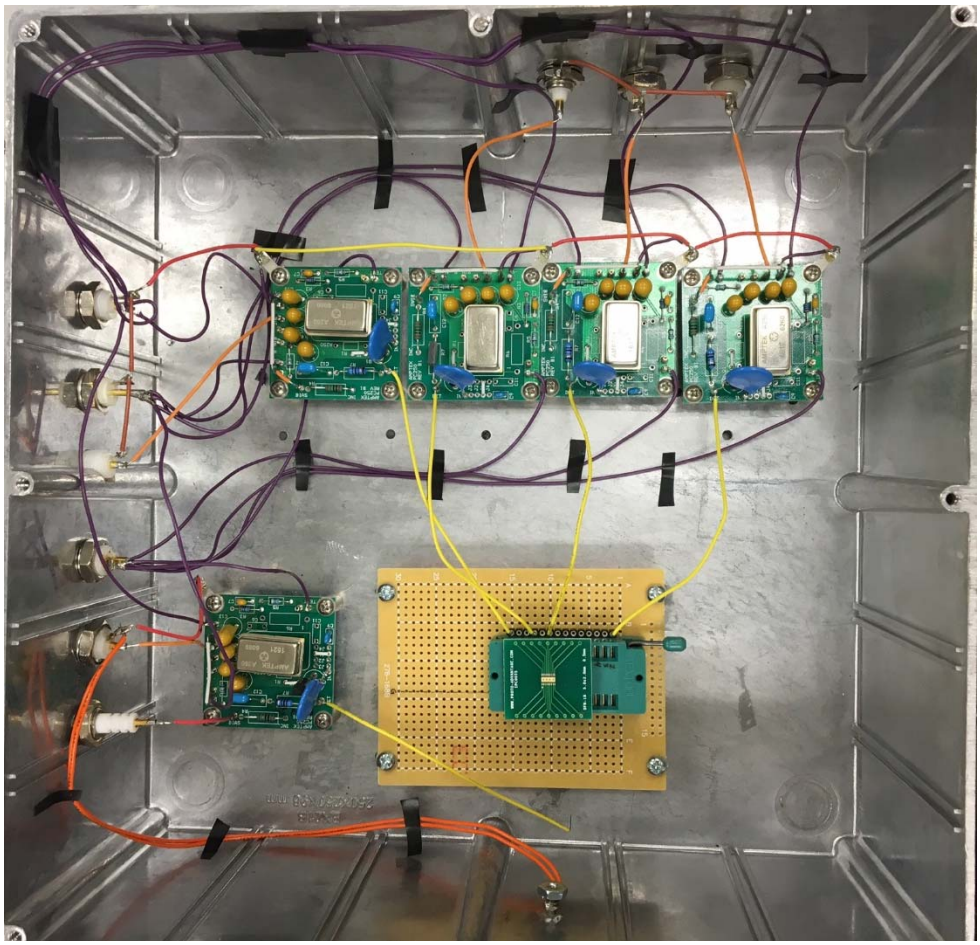

Figure 22: Depth correction testing electronics that allows the simultaneous readout of signal from the cathode as well as four anode pixels.

Objective 7: Assess Efficiency and Energy-Dependent Response Functions of BiI_3 Spectrometers

Through applying growth techniques tailored to reduce defects, the spectral performance of this BiI_3 has finally been realized through this work. Crystals grown with superheating gradients to suppress void formation have exhibited better spectral performance than ever before seen for BiI_3. For the first time, gamma ray spectra from > 100 keV source emissions have been obtained from high quality Sb:BiI_3 bulk crystals with limited concentrations of defects (point and extended). Two examples of gamma ray spectra obtained at room temperature from different samples grown with superheating gradients are shown in Figure 23. The spectrum shown in (A) was obtained from a 1000 ppm Sb-doped BiI_3 crystal biased to -2630 V/cm. A clear distinction between the 32 and 81 keV photopeaks can be observed from the ^{133}Ba spectrum along with the higher energy 302, 256, and 383 keV photopeaks that are largely convoluted. Low energy X-ray and gamma ray emissions were caught in the edge of the electronic noise tail, and as such, it is difficult to

accurately ascribe a resolution value to those photopeaks. The low signal-to-noise ratio in this sample can be attributed to its relatively low resistivity on the order of 10^8 Ω-cm. Nonetheless, the sample measured in Figure 23 (A) presented the first case in which a gamma ray source with multiple emissions produced a spectrum within a Sb:BiI_3 detector. The decay scheme and spectrum shown in (B) likewise show the emissions from a ^{241}Am source. The sample used to collect the ^{241}Am spectrum exhibited excellent photopeak discrimination at low energy. The detector's performance was enhanced by its higher resistivity of ~$5 \cdot 10^9$ Ω-cm, and demonstrated a resolution of 4.5% for the 59.5 keV gamma ray emission when biased to a field of -2275 V/cm. Additionally, the X-ray emissions from the Np decay product were clearly distinguishable alongside the gamma ray photopeak. The resolution presented here is a marked improvement over the 29% resolution recently reported for vapor transport synthesized BiI_3 [21].

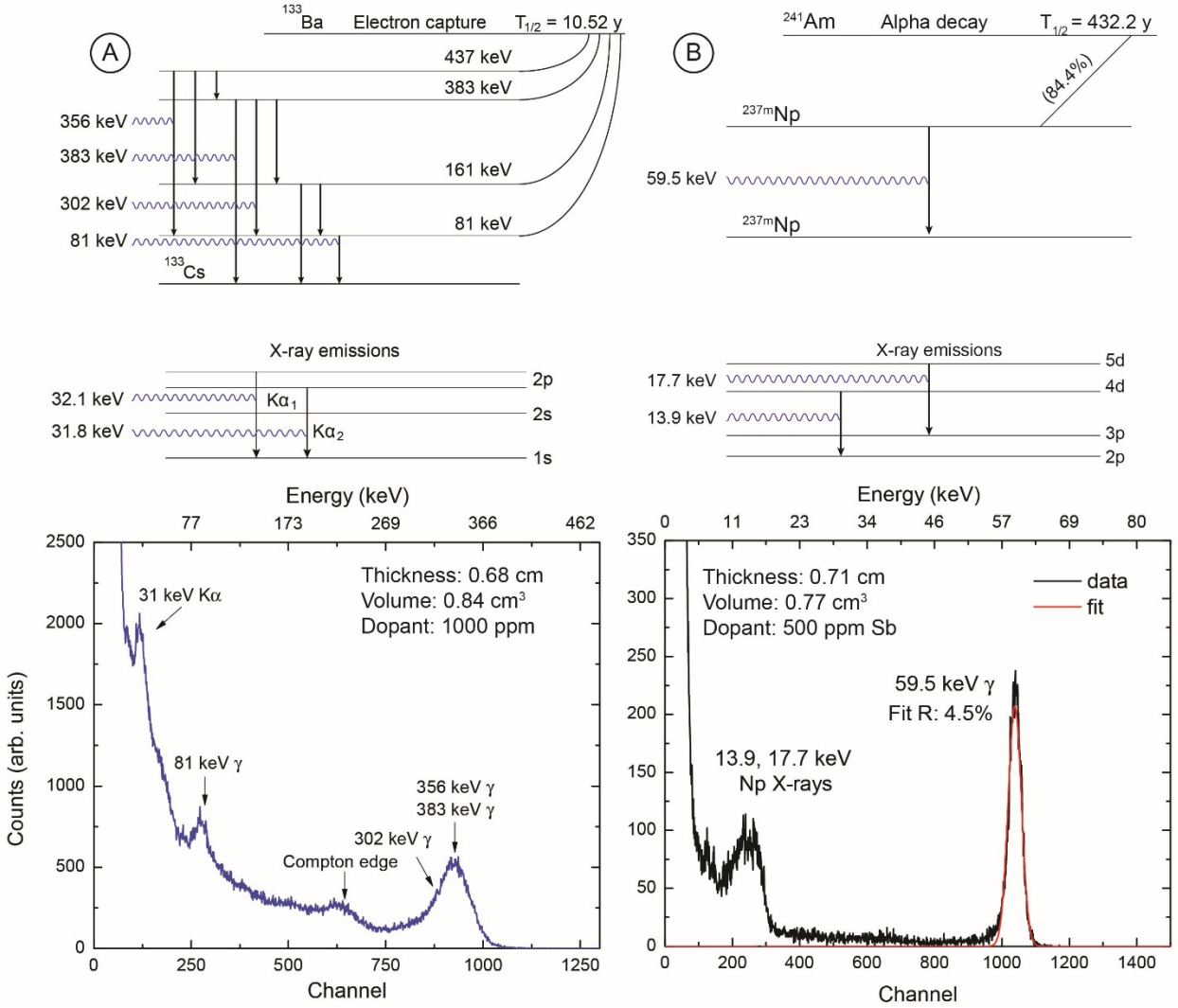

Figure 23. Spectra obtained from superheated BiI_3 crystals along with the corresponding decay scheme for the sources ^{133}Ba (A) and ^{241}Am (B).

Higher energy spectra are also capable of being obtained with good resolution from superheated BiI_3 crystals. Figure 24 shows the spectrum obtained by a ^{137}Cs source, which clearly exhibits a photopeak at 662 keV as well as Compton scatter features expected from partial energy transfer interactions. Plot (A) shows the entirety of the spectrum obtained, while (B) focuses on the photopeak. As is characteristic from many RTSD spectra at higher energies, the photopeak here features the presence of lower energy tailing. This deviation from the expected Gaussian shape of the photopeak implies that some degree of charge is still being quenched as it drifts through the crystal to the collecting electrodes. In a perfect semiconductor detector, all field line vectors begin at the planar cathode and end at the anode pixel; however, non-uniformities within the detector crystal such as dislocations, inclusions, grain boundaries, inhomogeneous surface and bulk conductivities, or electrode interactions can distort this idealized case [38, 39]. In the best cases, incomplete charge collection due to signal quenching results in a “tailing” effect on the photopeak. In the worst cases, as is seen in non-superheated crystals, the entirety of the charge generated in an ionization event becomes culled and the crystal loses its ability to output a spectra. In spectra (B) of Figure 24, the low energy tailing reduces resolution by 1%.

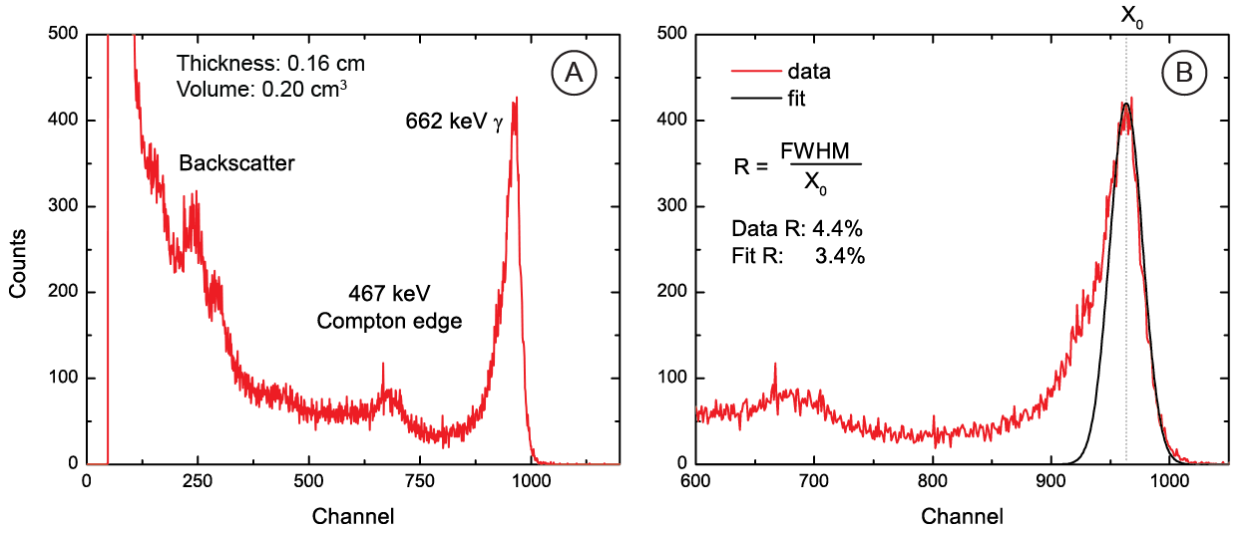

Figure 24. Spectrum obtained from a ^{137}Cs source. Plot (A) shows the entire spectrum while (B) focuses on higher energy features.

Due to the tailing effect on the lower energy edge of the photopeak, fitting resolution by the upper energy tail of the photopeak can be performed to realize the intrinsic resolution exhibited by a detector for a given energy. This method is known as fitting by the resolution at the full width upper half max (FWUHM). Figure 25 shows another ^{137}Cs spectrum collected from a different BiI_3 sample than that in Figure 24. In these spectra, the effect of low energy tailing from incomplete charge collection is observed to become more severe as collection time is increased from 660s

to 1200s. The resolution degrades by 0.6% over that collection period; however, the FWUHM derived resolution remains the same. Eliminating low energy tailing involves having tight control over atomistic defects that cause charge trapping within the band gap of a semiconductor. One method by which the negative tailing effect can be mitigated is through depth correction techniques, which normalize photopeak centroid channel among all interaction depths within the crystal.

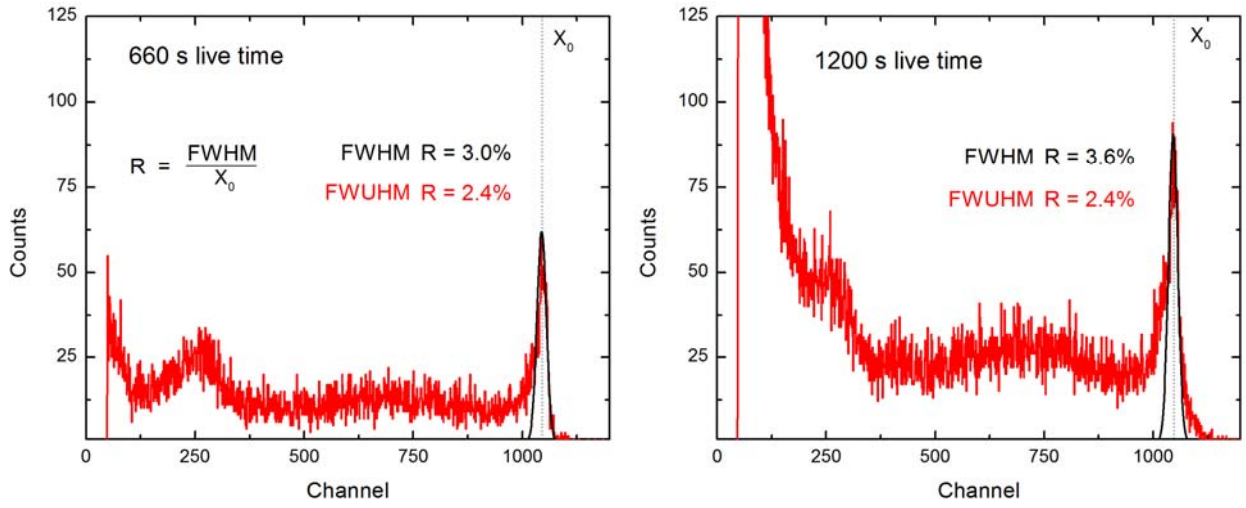

Figure 25. Comparison of signal obtained from a ^{137}Cs source for counting times of 660s and 1200s. Over time, the resolution of the photopeak degraded due to low energy tailing.

While the bulk of these superheated crystals are not entirely defect-free [2], the defect concentrations on the order of 100–300 voids cm^3, instead of several thousands, provides quality which allows for the acquisition of spectra. It is likely that further enhancements to crystal growth can reduce the levels of voids even further. It is foreseeable that in the future development of BiI_3 and Sb:BiI_3, the defect-free regions of the crystal will be milled out for detector utilization, similarly to the manner in which Te-inclusion free regions of CZT are harvested [40]. In this work, harvesting location within a crystal boule has become an important consideration for spectrometer grade crystal samples. Samples analyzed here were each taken from the cylindrical section of a crystal ampoule, and at least 1 mm away from both the beginning of the tip region and the last-to-freeze region. To ensure that the crystals analyzed in this work indeed possessed a limited concentration of defects, each sample was analyzed through IR microscopy before attempting to acquire spectra. For comparison between the local microstructure of the crystal and the spectral output, Figure 26 presents an IR micrograph of the region in a BiI_3 crystal along with spectra obtained from that location in the crystal. Micrograph (A) and micrograph (B) show the same region before and after the electrode was cleaved off, as highlighted by the yellow box. In the

area underneath the collecting anode pixel it is seen that there is a very low concentration of void defects. The plot in Figure 26 (C) shows a gamma ray spectrum obtained from the pixel area, highlighted in the micrographs, when biased to a field of -1980 V/cm.

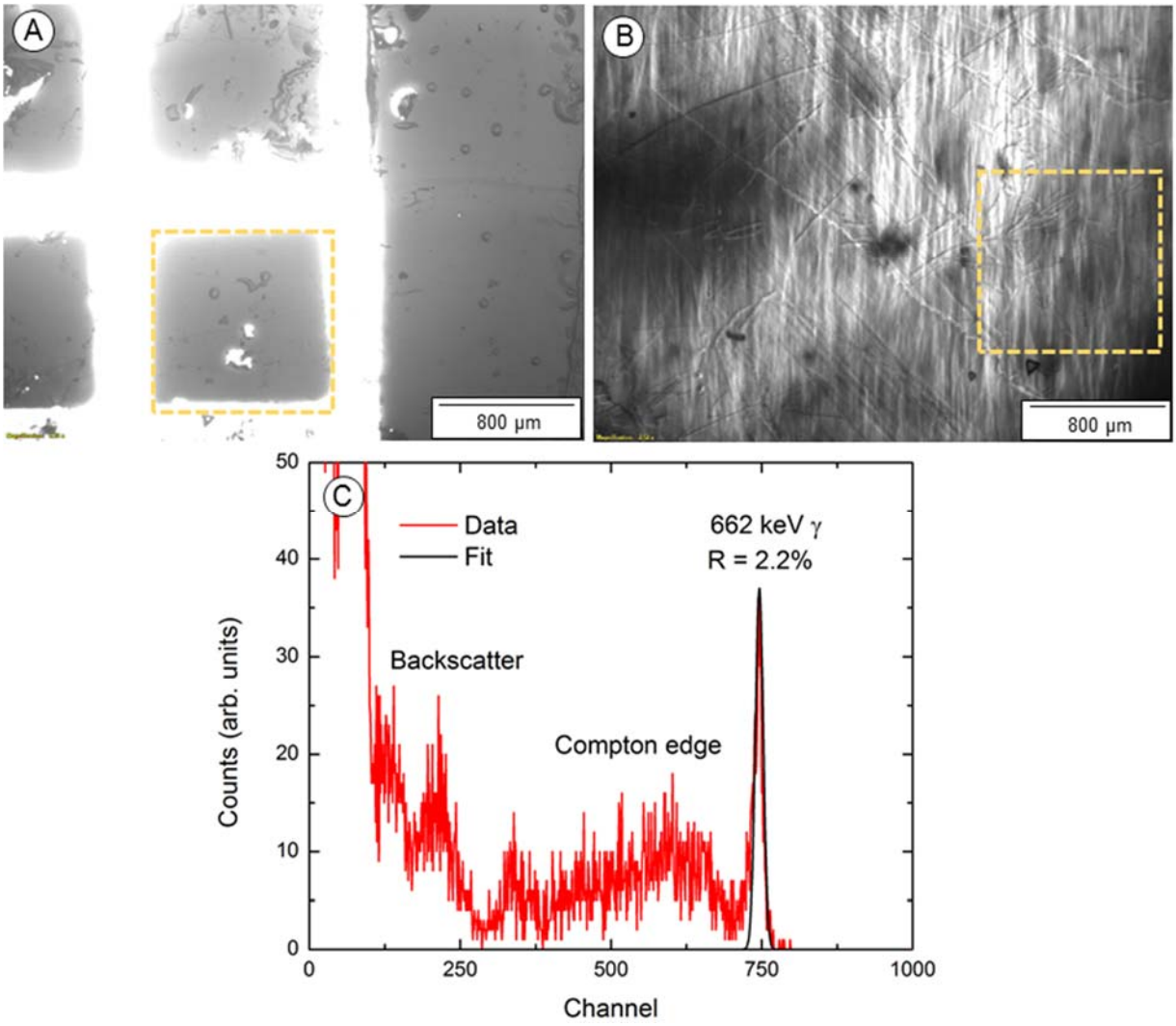

Figure 26. Comparative micrographs of a 1000 ppm doped Sb crystal with the pixel electrodes present (A) and removed (B). The bulk of this crystal is relatively void free, and resulted in the capture of the spectra presented in (C) from a ^{137}Cs source.

The defect deficient region allowed for the collection of the best-reported photopeak resolution for a BiI_3 detector. The spectra exhibited a very small degree of low energy tailing such that the FWHM, rather than the FWUHM, was used to calculate resolution of 2.2% for the 662 keV emission of ^{137}Cs. The photopeak centroid channels corresponded very linearly with gamma ray energy for the energy region between 31 and 662 keV, which implies that BiI_3 charge generation scales proportionally to gamma ray energy in the regime where many gamma ray energies are found.

Objective 8: Test Detector Performance under Environmental Conditions

The longevity of a spectrometer crystal in environmental condition is important to understand toward the development of an RTSD material. In this work, unencapsulated BiI_3 crystals were characterized following long-term biases in ambient air conditions. Figure 27 shows some of the effects that oxidation causes on non-encapsulated crystals. Through IR microscopy of biased BiI_3 samples, some samples exhibited a dark haze-like features within their bulk. Cleaving the sample using adhesive tape revealed through visual inspection that two planes near the center of the sample easily delaminated and showed a dark brown film coating the (001) planes. Optical micrographs of the film gave evidence that an oxide or oxyiodide phase formed only on the one interfacial layer of BiI_3.

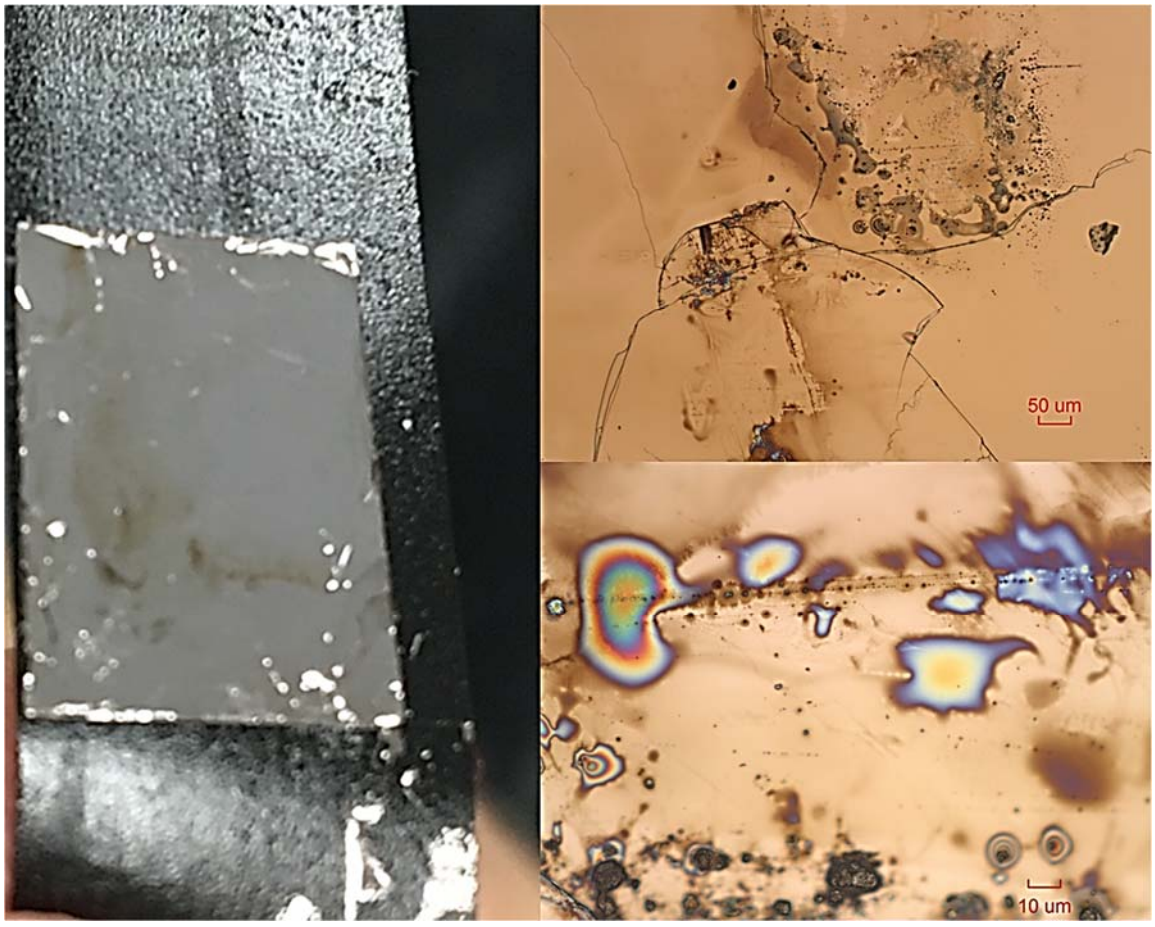

Figure 27. The cleaved Bi surface where extended defects were located. Two different reactions were identified.

To determine the chemical identity of the layer, Raman spectroscopy was performed to match a vibrational mode spectrum to the signature of the unknown phase. The spectrum

obtained from the sample is shown in Figure 28 with an inset showing the spectrum obtained from a fresh BiI_3 crystal. Two vibrational modes appear in the spectrum of the reacted sample at 84.3 and 149.0 cm^{-1}. These modes match those obtained in spectra for the compound BiOI as shown by Kazyrevich *et al*. [41] and Fang *et al*. [42].

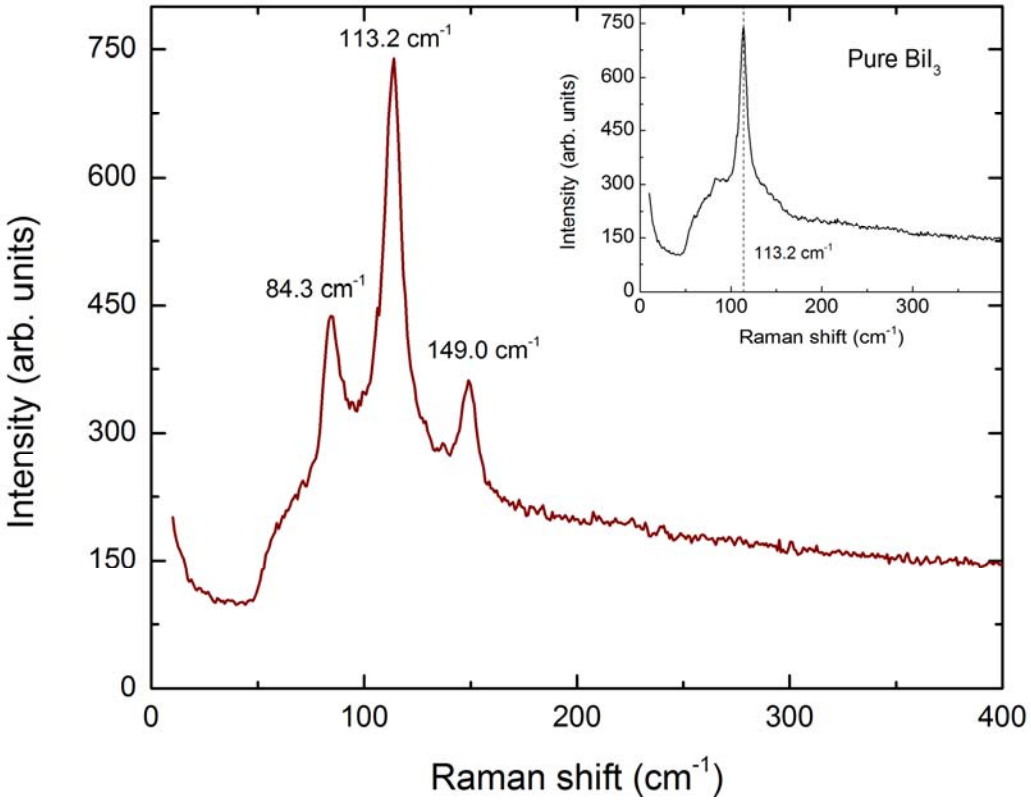

Figure 28. Raman spectrum obtained from S21 following a 2000 V bias applied for 7 days. Inset shows the Raman spectrum of BiI_3.

While these artifacts of environmental exposure under bias are deleterious to the electronic performance of the material, they are easily remedied by capping the crystals with epoxy. When crystals are epoxy capped, they still exhibit breakdown in electronic performance after extended periods of bias, but they do not show the offset of Ohmic behavior and the BiOI phase.

Objective 9: Assess Radiation-induced Performance Degradation

When BiI_3 is subjected to a strong electrical bias, after some time has passed the electronic performance of the crystal begins to break down. This effect is referred to in literature as “polarization” [21, 22, 24-26], and results in a degradation of resistivity, increase in leakage

current, and overall loss of the ability to acquire spectra. In this chapter, polarization is investigated and characterized to gain insight into the mechanisms contributing to failure in polarized samples. In doing so, a better understanding of the underlying phenomena that contribute to sensor breakdown is gained, and potential methods by which detector lifetime can be improved are identified.

Throughout BiI_3 literature the presence of polarization phenomena has been reported after both short and long-term bias [22, 24, 25]. An example of the effects from polarization are seen in Figure 29 (A) and (B). Plot (A) shows the evolution of a ^{137}Cs spectra over the course of an overnight measurement, where each spectra is saved in 10-minute increments. The photopeak centroid channel of a 662 keV photon is observed to shift by 10 channels over several hours over the time when bias was applied to the detector. The 10-channel shift corresponds to a difference of 48.8 mV of induced charge output by the preamp. When taking into account the gain introduced in the signal processing, this shift also corresponds to an average of 3,500 fewer electrons inducing their total charge onto the anode. Figure 29 (B) highlights the more severe effect of polarization. The average count rate from an ^{241}Am source was monitored in 10 minute intervals over several hours. Between 1 hour and 6.5 hours the count rate was relatively stable, with more-or-less thermal noise causing some occasional spread in the count rate. However, after approximately 6.5 hours the count rate began to drastically increase, and after 7.5 hours the detector lost all ability to produce signals from gamma rays.

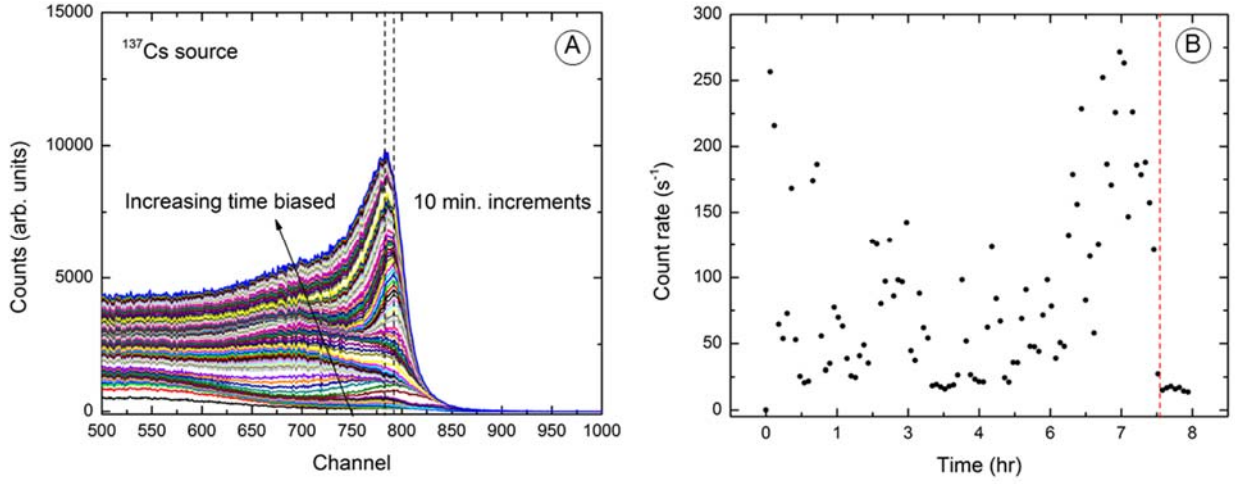

Figure 29. (A) Shift in photopeak centroid channel vs. the amount of time the detector was subjected to bias. (B) Count rate vs. time for a BiI_3 detector exposed to a ^{241}Am source. After an extended time under bias, the ability to detect ionized charge fails due to polarization phenomena.

To examine polarization, a number of BiI_3 samples electroded with planar Au contacts were biased at field conditions greater than (±) 2500 V for weeklong periods. In each case, the I-V behavior of the samples were observed to deteriorate following the bias. Figure 30 presents representative current density vs electric field data obtained before and after the week-long of bias of one sample. The original I-V behavior of the sample was Ohmic, and exhibited high resistivity of 1.07 x 10^{10} Ω-cm, however the resistivity decreased by over an order of magnitude following the bias application. Along with the decrease in resistivity, non-Ohmic behavior was observed in the positive electric field regime in the sample following the bias. These findings indicate that an internal potential barrier or accumulation of space charge arose in the sample following the bias application.

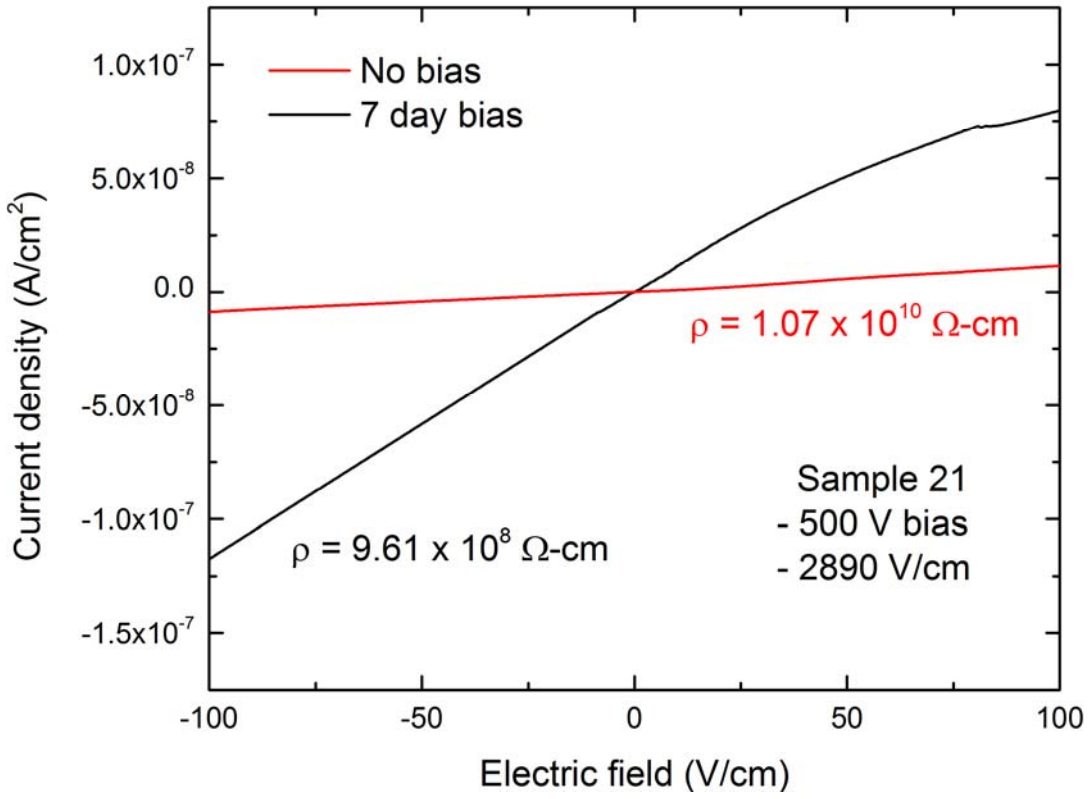

Figure 30. Current density vs. electric field curves comparing behavior before and after the crystal was biased for 7 days.

In addition to the breakdown of electronic performance, the samples that were subjected to extended bias exhibited interesting physical deformation features. A representative sample, shown in Figure 31, developed “bubble”-like protrusions underneath the anode surface after the extended bias period. These features did not appear on the cathode side of the sample. The finding of these features on only the positively charged anode surface, along with the breakdown in Ohmic behavior seen in the forward bias regime, indicates an anionic defect species produced

the features observed in the sample. The hypothesis formulated following these findings was that iodine, volatilized over the extended time under bias, builds up at existing microstructural defects and delaminates the (001) planes to create the “bubble” features.

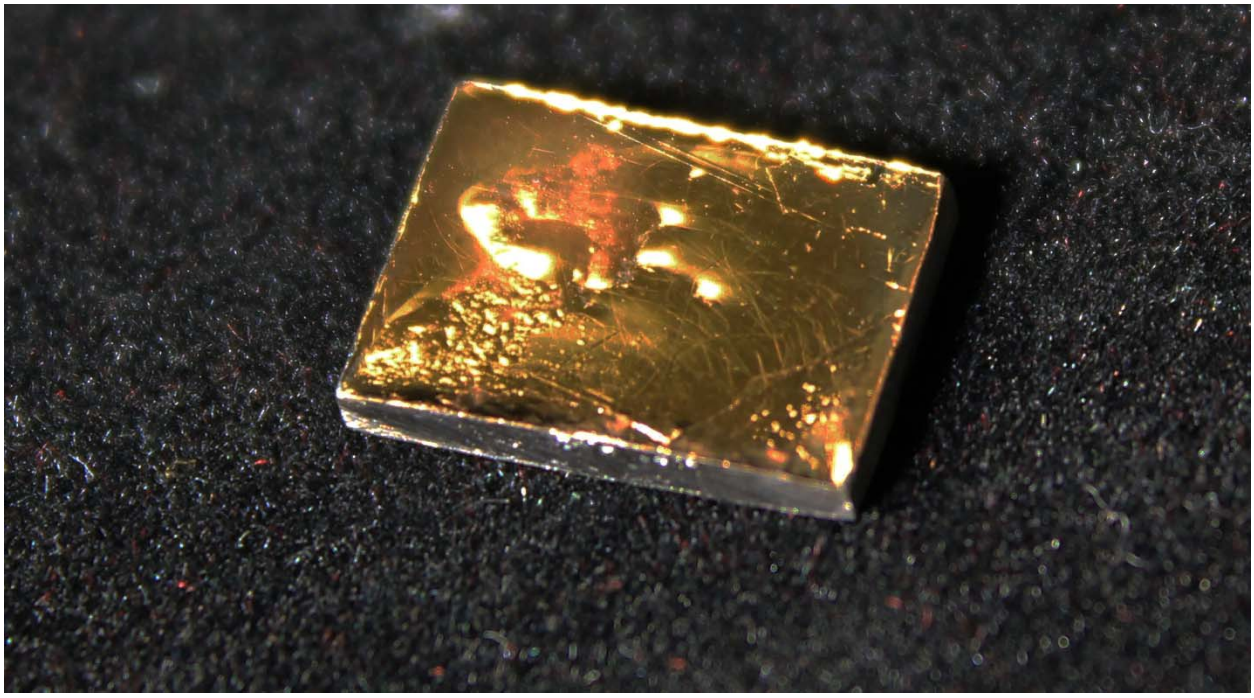

Figure 31. BiI_3 crystal biased for 7 days. Bubble-like features on the top electrode indicate delamination within the bulk of the crystal. Image contrast enhanced to accentuate features.

Examination of the contribution to polarization from anion drift in BiI_3 was performed by analyzing a sample of BiI_3 doped with Br as an anion iodine surrogate. Time of flight secondary ion mass spectrometry (ToF-SIMS) was performed on the anode surface of the Br-doped BiI_3 sample, providing the data shown in Figure 32. The first image in each column shows the secondary electron image of the surface, the second image shows the concentration of Br found by the fifth raster of the surface, and the final image shows an HSI (hue, saturation, intensity) plot of the ratio of ^{79}Br to ^{127}I. The color chart on the images show regions that are Br-deficient as blue, and regions where Br is more concentrated as red. When accounting for the 50.69%/49.31% abundance ratio of 79Br to 81Br, the concentration of Br/I was found to be 0.0164 ± 0.0033 for region A, 0.0149 ± 0.0059 for region B, and 0.0153 ± 0.0046 for region C. The ToF-SIMS analysis on the anode surfaces showed that, apart from the scratch/clump regions, the Br:BiI_3 lattice exhibited a rather homogenous ratio of Br/I. Averaging the data from all three regions, it was found that for every 10,000 atoms of iodine in the lattice, 155 ± 8 atoms of Br were present.

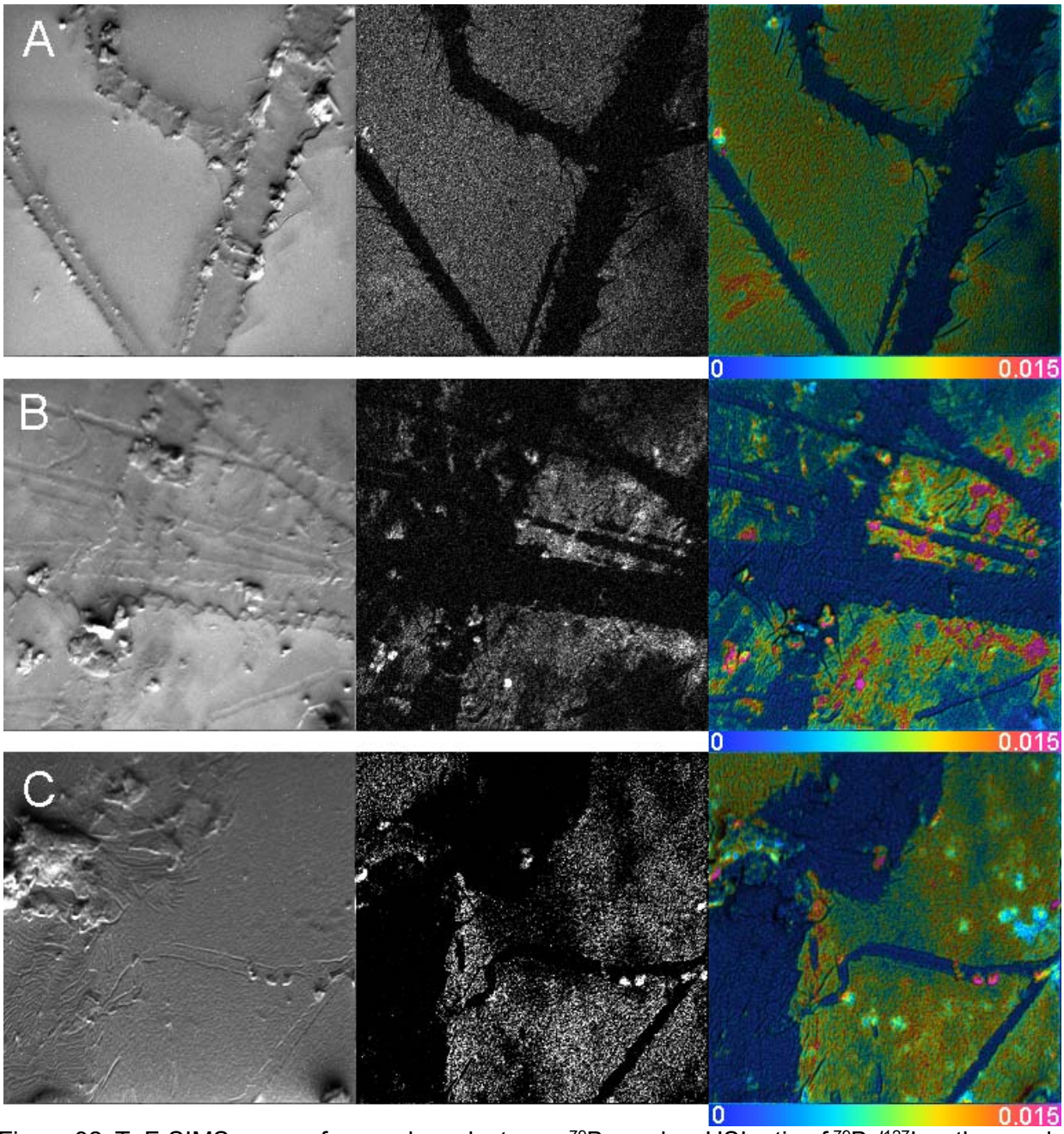

Figure 32. ToF-SIMS scans of secondary electrons, ^{79}Br, and an HSI ratio of $^{79}Br/^{127}I$ on the anode surface of a Br:BiI_3 sample biased to ~8000 V/cm field for a period of seven days.

In stark contrast to the anode Br/I findings, as shown from Figure 33, the cathode surface exhibited much more homogeneity and an overall lower concentration of Br. Analysis of the Br/I ratio from random regions of interest on the cathode surfaces showed the Br/I ratios were found to be 0.0050 ± 0.0013 for region A, 0.0061 ± 0.0017 for region B, and 0.0047 ± 0.0017 for region C. Overall, on the cathode surface, for every 10,000 atoms of iodine, 53 ± 7 atoms of Br were

found. The stark contrast in Br concentration between the anode and cathode surfaces provides supporting evidence for the drift of iodine in the presence of extended periods of bias.

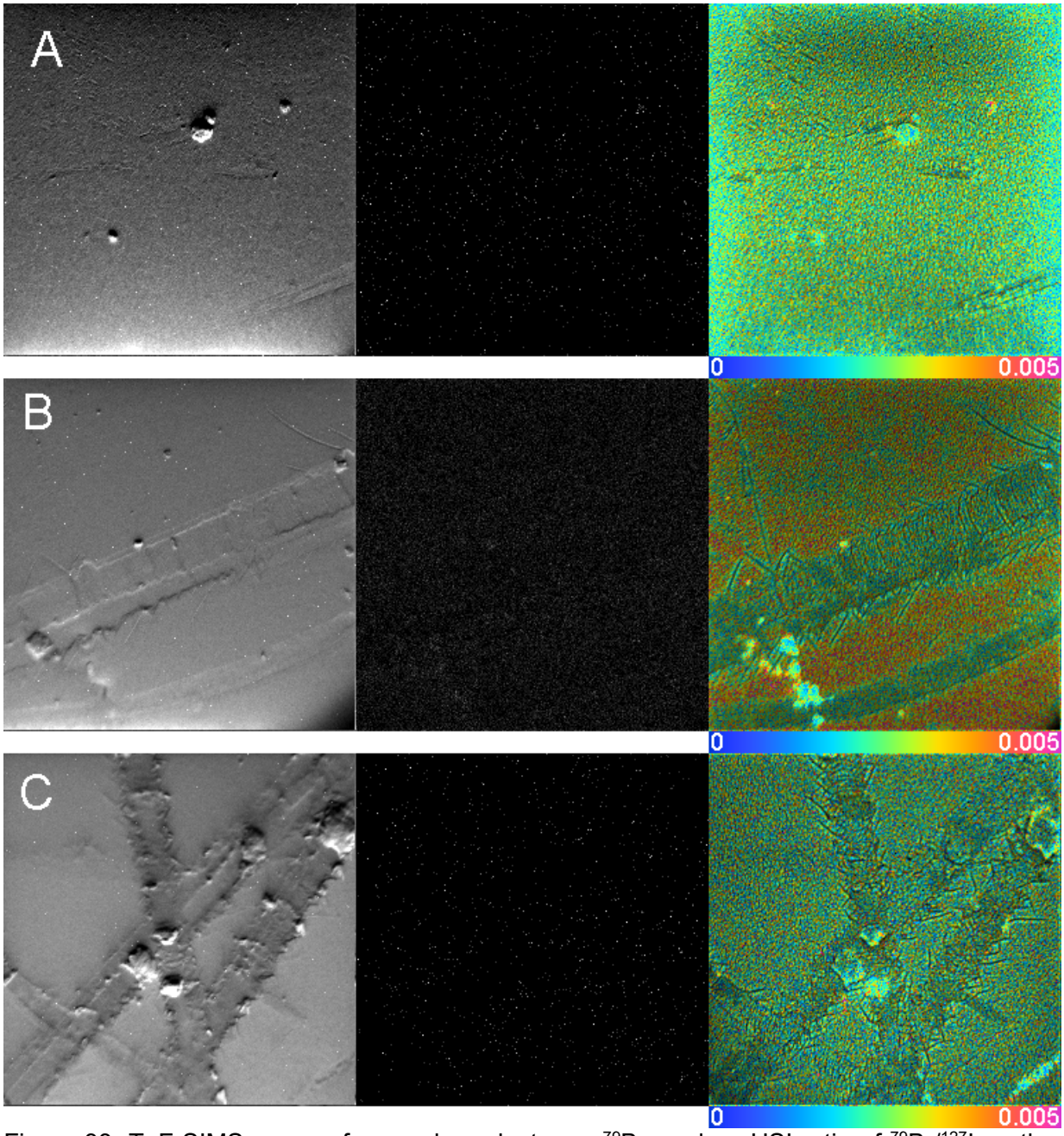

Figure 33. ToF-SIMS scans of secondary electrons, ^{79}Br, and an HSI ratio of $^{79}Br/^{127}I$ on the cathode surface of a Br:BiI_3 sample biased to ~8000 V/cm field for a period of seven days.

Box plots presenting the data obtained from ToF-SIMS analysis of each surface are presented in Figure 34. To complement the analysis, a two sample t-test on whether the means of the two samples were equal provides a P-value on the order of 10^{-14}, strongly indicating that the Br/I ratio was statistically different in each case.

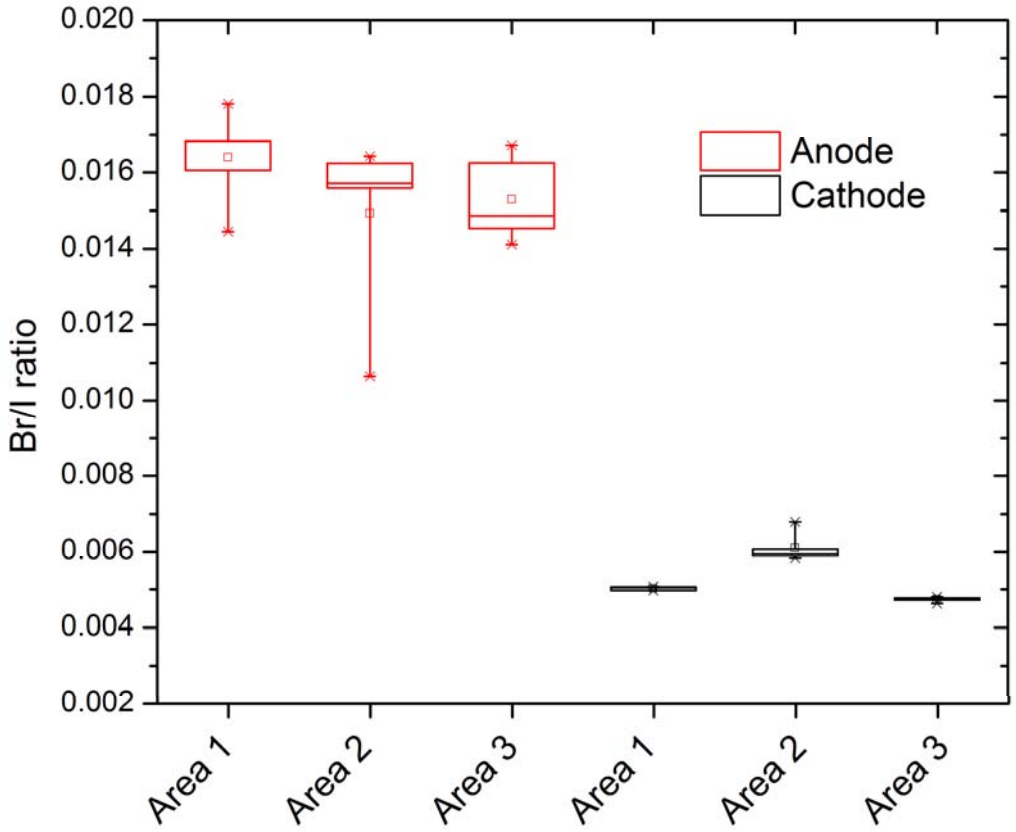

Figure 34. Box plots showing the Br/I ratio from the data obtained in the ToF-SIMS analysis of the Br:BiI_3 anode and cathode surfaces.

The success in using Tl electrodes to alleviate polarization in TlBr inspired a similar approach in BiI_3 by using metallic Bi as an electrode. A Bi target (99.99%, American Elements) was used to sputter Bi onto the (001) surface of several samples of BiI_3 under 0.08 mbar Ar. Conductivity of the surface was verified using a probe station to test the connection between different points on the Bi-coated (001) surface. The conclusion of the study on Bi-electroded samples showed no improvement in polarization compared with the Au-electroded samples. Unfortunately, the solution that worked with TlBr did not work with BiI_3. It is possible that surface interaction between the Bi metal and the iodine-terminated BiI_3 surface prevent the recombination of free I^- or I_2 back into BiI_3. Future studies will attempt to anneal Bi-electroded samples in the presence of an iodine atmosphere in an attempt to enhance surface adhesion of the Bi electrode.

Objective 10: Assess Detector Performance in a Scalable Mixed-field Environment

Multiple BiI_3 crystals were irradiated by thermal neutrons produced by the Argonaut-type reactor at UF. Samples were doubly encapsulated in polyethylene bags and an aluminum capsule. Before sealing, each crystal was weighed by a scale calibrated using an ASTM Class 1 10 g weight. After being weighed and sealed, the aluminum capsule was lowered into the shield tank of the UFTR (the highest neutron flux position in the reactor) where it was irradiated by neutrons. This position is highlighted in Figure 35 showing a diagram of the the UFTR. The water tank was used as a heat sink for the samples to ensure that no changes to the samples were due to thermal effects. After irradiation, the activity of the samples was measured using a high purity germanium (HPGe) detector. I-V measurements were performed on the samples before and after irradiation. Multiple sets of samples were irradiated at power levels of 0.1, 1, 10, and 100 kW for 30 minutes.

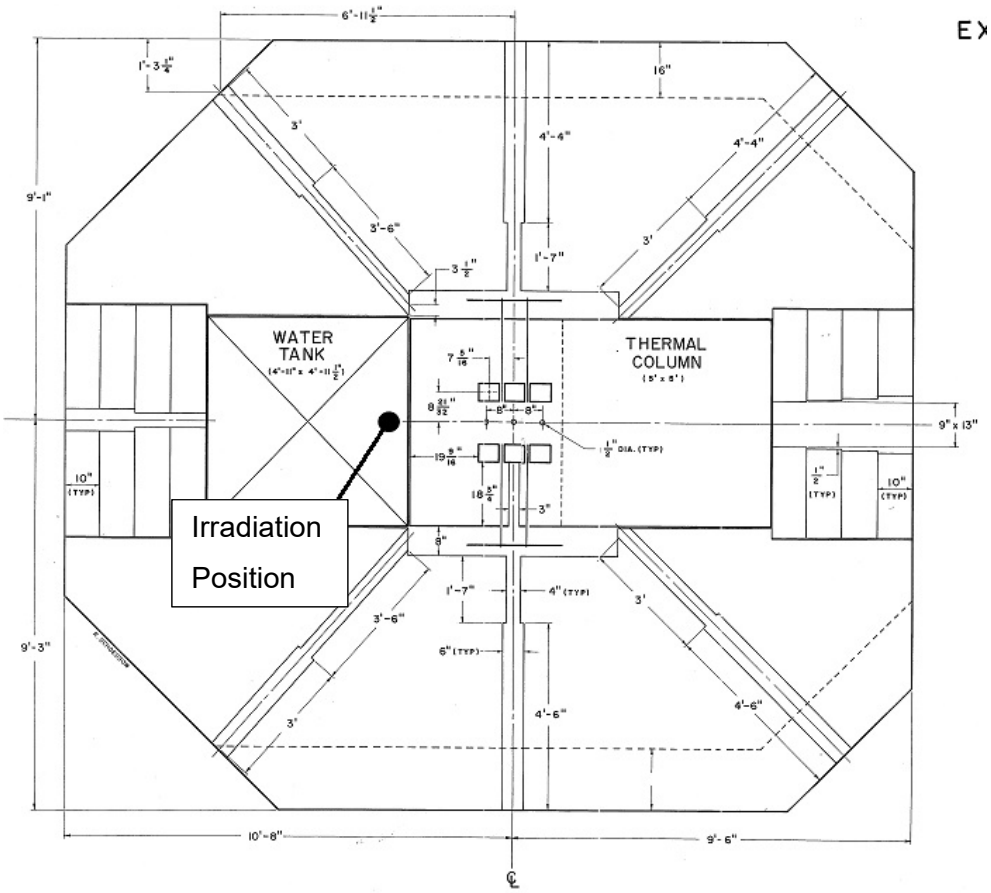

Figure 35. Argonaut-type Reactor cross-section with neutron irradiation position of BiI_3 crystals shown.

For these irradiations, one of the concerns was the possibility of release of radioactive iodine, due to the bioavailability of radioiodine. The shield tank that the experiments took place in provided for a temperature controlled environment as the tank is over a thousand gallons and the water is circulated by a pump. Previously, iodine was observed to be coating the bag when irradiating some samples outside of the water tank. There was no sign of iodine release at any power level. These post-irradiation results are shown in Figure 36 and Figure 37. In addition to no visual sign of iodine release, there was no sign of mass change for any sample.

Figure 36 - Samples 16, 18, and 43 still sealed in polyethylene after irradiation at 0.1 kW

Figure 37 - Samples 17, 24, and 47 still sealed in polyethylene after irradiation at 1 kW

Following irradiation, the activity of all samples was measured using an HPGe detector. Samples were placed inside of a lead shielded container to reduce background radiation interference with measurements. The characteristic peak of 442 keV produced by the activated iodine isotope, I-128, was clearly seen in all measurements. IV measurements for each sample were performed before and after irradiation using a Keithley electrometer. The irradiated BiI_3 crystals showed notable degradation in their IV results, marked by resistivity loss and offsets from Ohmic behavior. Examples of this are shown in Figure 38. These tests highlight the poor suitability

of BiI_3 as a neutron detector. The atomistic defects caused by neutron damage severely affected the electronic behavior of the BiI_3 crystals.

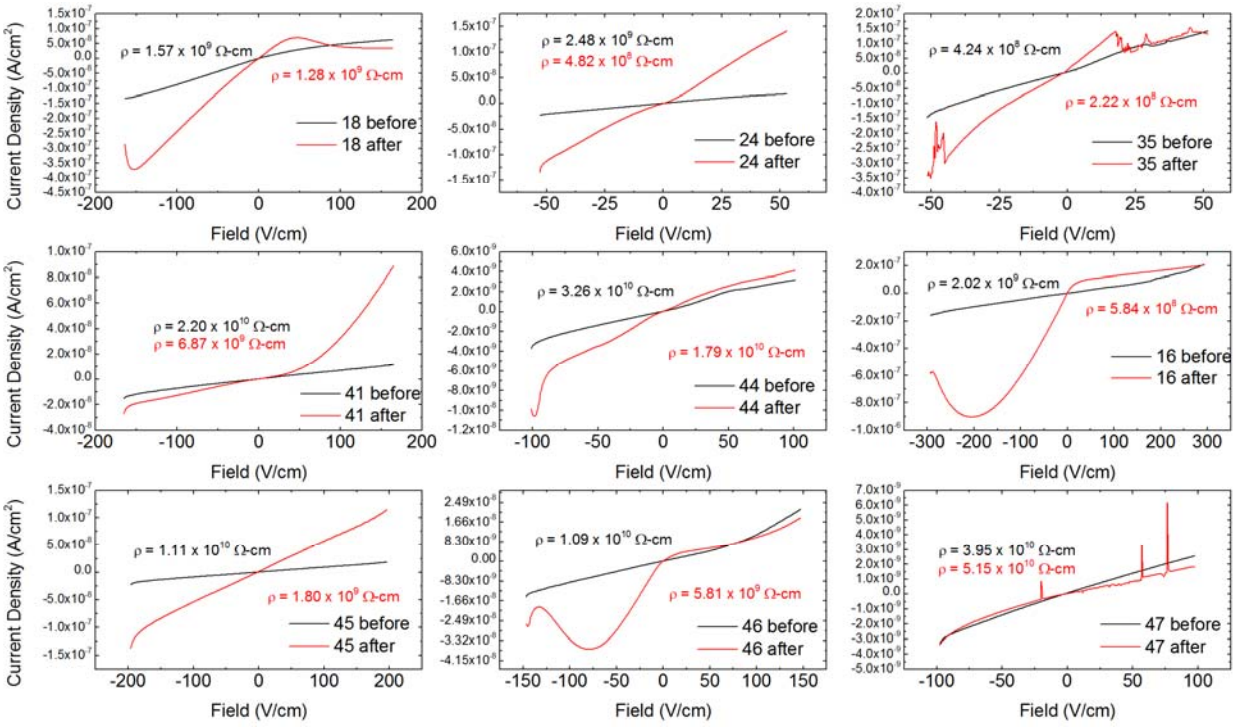

Figure 38. I-V behavior of BiI_3 crystals before and after neutron irradiation in the UFTR.

Objective 11: Measure Spent Fuel

Spent fuel was measured with BiI_3 spectrometers side-by-side with a commercial eV Products SPEAR detector. Measurements were performed at the radiochemical processing laboratory at Pacific Northwest National Lab. Two used fuel samples were measured in this work, designated as “109-HBU 539-B3”, “ATM-109-carbonate”. The 109-HBU 539-B3 and ATM-109 carbonate fuel measured in these experiments initially consisted of 3% enriched ^{235}U, and were irradiated between February 1979 and September 1987, and then a second time between November 1989 and September 1992, in the Quad Cities 1 BWR [43, 44]. In total, these fuel sections were exposed to between 60 and 75 GWd/MTU burnup and 3508 on-power reactor days. Both samples were taken from the same rod, and were additionally doped with 2 wt% Gd_2O_3 burnable poison. The ATM-109-carbonate sample consisted of a section of the 109-HBU fuel dissolved in an ammonium carbonate/hydrogen peroxide mixture. The resulting sample consisted of a solution of $UO_2(CO_3)_3^{4-}$ in which most actinides are soluble. The ATM-109-carbonate sample is particularly useful to characterize towards safeguards applications, because its emission spectrum is representative of high burnup fuel dissolved to be reprocessed. The low density liquid

state of the sample allows many more emissions to be transmitted than a dense oxide fuel pellet. The ATM-109 used fuel samples have been characterized in other works using HPGe detectors [43, 45, 46], and major element concentrations were found via mass spectrometry in the work by Rodriguez *et al.* [45].

Figure 39 presents the background corrected gamma ray spectrum acquired from the highest activity spent fuel source examined, 109-HBU 539-B3, which gave an exposure rate reading of 2000 R/hr at 72 cm from the source. At a 175 cm source-to-detector distance, count rates from this source were in excess of 10,000 cps and yielded an average detector dead time of 7.7%. The principle emissions from this source were the actinide K_α and K_β X-ray emissions. Peak 1 in Figure 39 is centered at the 98.4 keV U K_α X-ray, and corresponds to the buildup from the K_α X-ray emissions of Th, U, Np, and Pu. Peak 2 signifies the K_β transitions from the respective actinides. Due to the pulse pileup associated with the high count rate, the resolution of the individual emissions from the K_α and K_β transitions were convoluted into single peaks. The only gamma rays seen in the ATM-109 sample are the ^{137}Cs photopeak at 662 keV, and the shoulder coming from the 185.9 keV emission of ^{235}U. Additional features in this high count rate spectra include an escape peak, marked as feature 3.

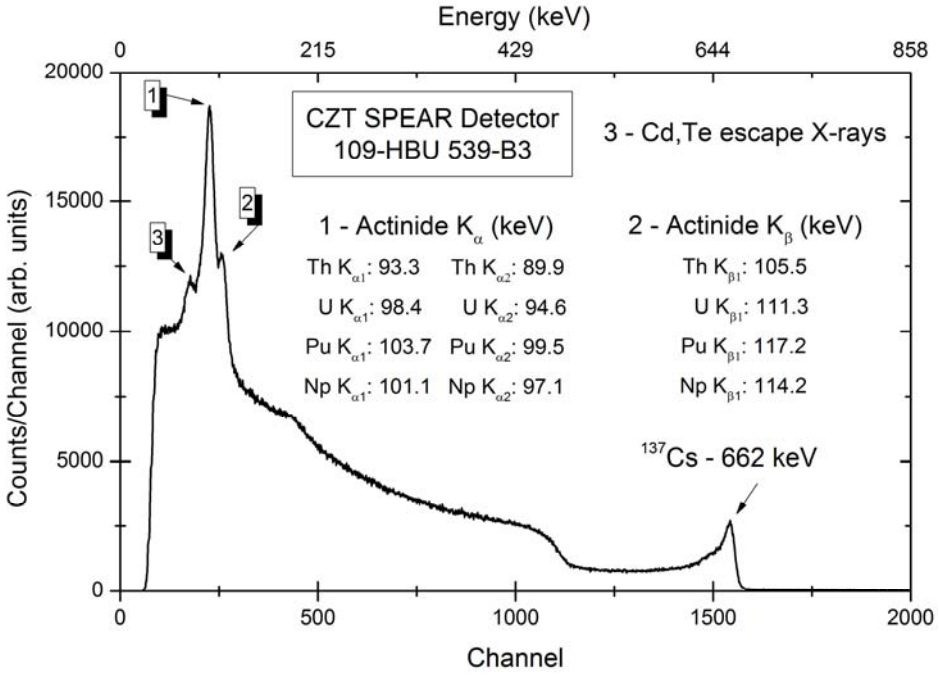

Figure 39. Spectrum acquired from spent fuel source 109-HBU 539-B3 from a CZT SPEAR detector. Labeled are the K_a and K_b X-rays, escape peaks, and gamma ray features that make up the spectrum.

The gamma ray activity, *I*, from a single fission product can be found through the relation

$$I = \varepsilon k S N \lambda e^{-\lambda T}, \quad (3)$$

where ε is the absolute detector efficiency, *k* the branching ratio for the decay, *S* the attenuation between the source and detector, *N* the number of fission product nuclei, λ the decay rate of the radionuclide, and *T* the cooling time [47]. Fitting a Gaussian function to the ^{137}Cs photopeak and accounting for the dead time of the detector provides an adjusted net count rate of 393 cps from the photoelectric effect interactions of the 662 keV gamma ray. The intrinsic efficiency of a 5 mm^3 CZT crystal was found by Quam to be approximately 0.00238 [48], and the photopeak efficiency for CZT detector arrays was found by Manini to be between 0.17 and 0.07 [49]. Using the experimental geometry to determine absolute detection efficiency, and inserting the values for the decay of ^{137}Cs into the variables of Equation (3) gives a ^{137}Cs fission product inventory in the sample of 8.35 x 10^{19} atoms.

Burnup, in atom %, can be predicted by the number of fission product nuclei present in a used fuel sample by the relation

$$BU = 100 * \frac{\cdot\cdot}{YU}, \quad (4)$$

where *Y* is the yield of the fission product and *U* is the number of initial uranium atoms in the sample. The total mass of the sample ATM-109 (fuel + cladding) was found to be 58.2 g [50]. If the mass of the UO_2 within ATM-109 is assumed to be 50 g, as was done in the analysis by Fast *et al.*, then the burnup predicted by the SPEAR detector from the ^{137}Cs present in the sample is 8.03 at%, or ~77 GWd/MTU. This estimate falls just above the upper estimate of burnup in the ATM-109 samples found in other works, but shows the usefulness of CZT as an RTSD for estimating burnup in used nuclear fuel.

Figure 40 presents the spectrum acquired from the ATM-109 carbonate spent fuel sample. The entire spectrum is presented in the top portion of Figure 40 while the bottom focuses on the spectral region between 30 and 130 keV. The carbonate sample exhibited a 1500 cps count rate, and featured a dead time much lower than the oxide of 1.14%. This spectrum contains several interesting features not seen in the solid fuel pellets analyzed, primarily due to the low density of the carbonate/peroxide solution relative to the oxide samples. The peaks labeled 1 through 9 each correspond to a specific measurable emission originating from either characteristic X-rays from the actinides, or the decay gamma transitions of the fuel radionuclides. Peaks 1 through 4

were attributed to the low energy gamma ray emissions of ^{238}Pu, ^{239}Pu, ^{240}Pu, ^{234}U, and ^{234}Th. Self-absorption from the high density of oxide pellets make these low energy gamma rays difficult, if not impossible, to resolve in normal used fuel measurements. The peaks labeled 5 through 9 correspond to the X-ray transitions of U, Pu, Am, and their daughter decay products. The 129 keV gamma ray emission from ^{239}Pu overlaps in energy with the K_β transition of Am, however due to the lack of an additional ^{239}Pu peak at 414 keV, it is possible that the peak is from Am alone. At higher energies, the gamma ray emissions from ^{235}U and ^{137}Cs were seen. In this spectrum, the ^{235}U peak at 185.9 keV was better resolved than in the oxide sample.

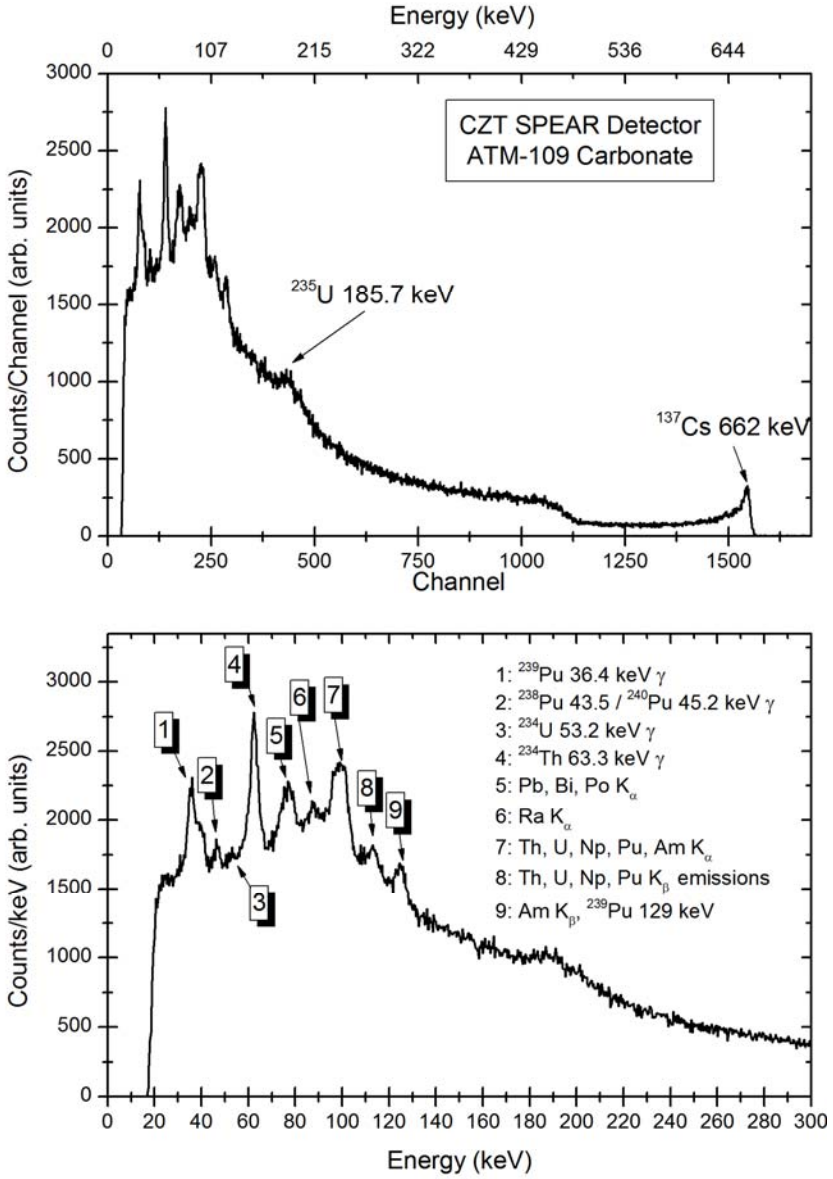

Figure 40. Spectrum acquired from spent fuel source “ATM-109 (carbonate)” from a CZT SPEAR detector. The top spectrum shows the entire range of spectral features while the bottom focuses on the low energy peaks.

Objective 12: Compare Spectral Data

The measurements taken by the CZT SPEAR detector were repeated with BiI_3 crystals integrated into a circuit consisting of an Amptek A250 preamplifier and a LabZY digitizer. These measurements represent the first ever “field test” for BiI_3 spectrometers. Electrodes on the BiI_3 samples were applied in a pixel grid on the anode side, and a pogo-pin connection was used to connect the shaping electronics and the pixels. It was found that some pixels exhibited sensitivity to the used fuel sources while others did not have any response at all. Possibly some issues with electrode adhesion or localized damage were behind the effect. The ATM-109 oxide sample measured by CZT is shown in Figure 41 for a BiI_3 crystal biased to -1150 V. In this 5-minute count, the dead time of the detector was below 0.02%, which showed that the absolute detection efficiency was several orders of magnitude behind the commercial CZT detector. Due to this, a photopeak from the ^{137}Cs source never fully resolved during the collection time, however a shoulder from the Compton interactions was present at the higher channels. Two low energy photopeak features were seen in the spectrum, which were ascribed to X-rays originating from the actinide K_α and K_β as were seen in the CZT sample. Due to the lack of any well-known spectral features, an energy calibration could not be performed on the spectrum. While the crystals were not able to resolve a ^{137}Cs photopeak for burnup estimation, the ability to resolve the higher intensity actinide X-ray emissions is a remarkable feat for the first time BiI_3 has been used to characterize used fuel samples.

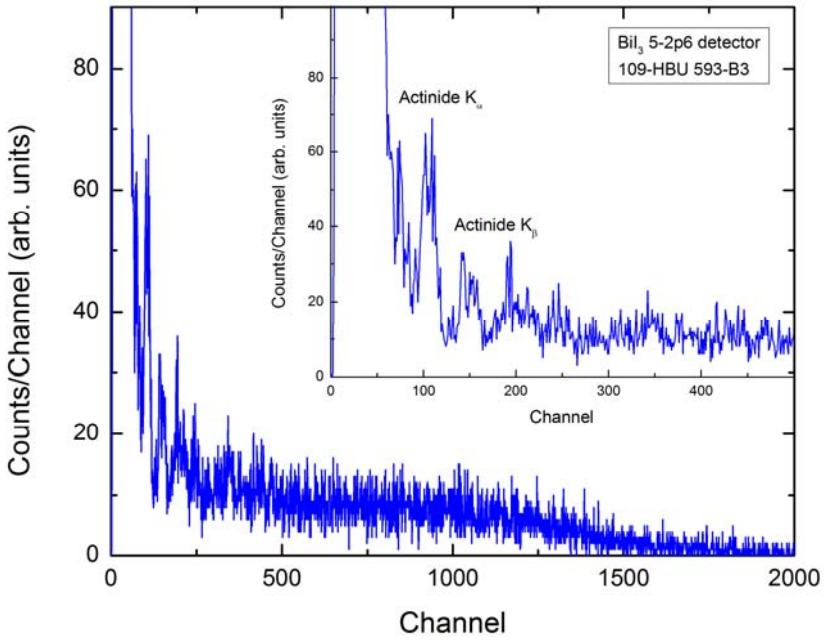

Figure 41. Gamma ray spectrum from the ATM-109 sample acquired with a BiI_3 crystal biased to -1150 V.

The ATM-109 carbonate sample measured with BiI_3 provided a much more interesting spectrum than the oxide. A spectrum measured from a crystal again biased to -1150 V is presented in Figure 42. This spectrum contains many features that closely resemble the spectrum measured by CZT. Six features are presented in Figure 42 which correspond to the low energy gamma ray emissions of ^{238}Pu, ^{239}Pu, ^{240}Pu, and ^{234}Th as well as the K_α and K_β emissions of the heavy actinides. While the actinide X-rays in this spectrum were not able to be separated into the elements which emitted them, several peaks were distinguished in the spectrum. Again, the absolute detection efficiency in this sample was much lower than the commercial CZT detector. Improvements to crystal growth, and lowering the defect concentration (atomistic and macroscopic), would improve the absolute detection efficiency and resolution in gamma ray spectra. Overall, while BiI_3 exhibited poorer performance than the CZT detector, the ability for BiI_3 crystals to resolve spectral features from used nuclear fuel is a marked achievement in the development of this material for safeguards purposes.

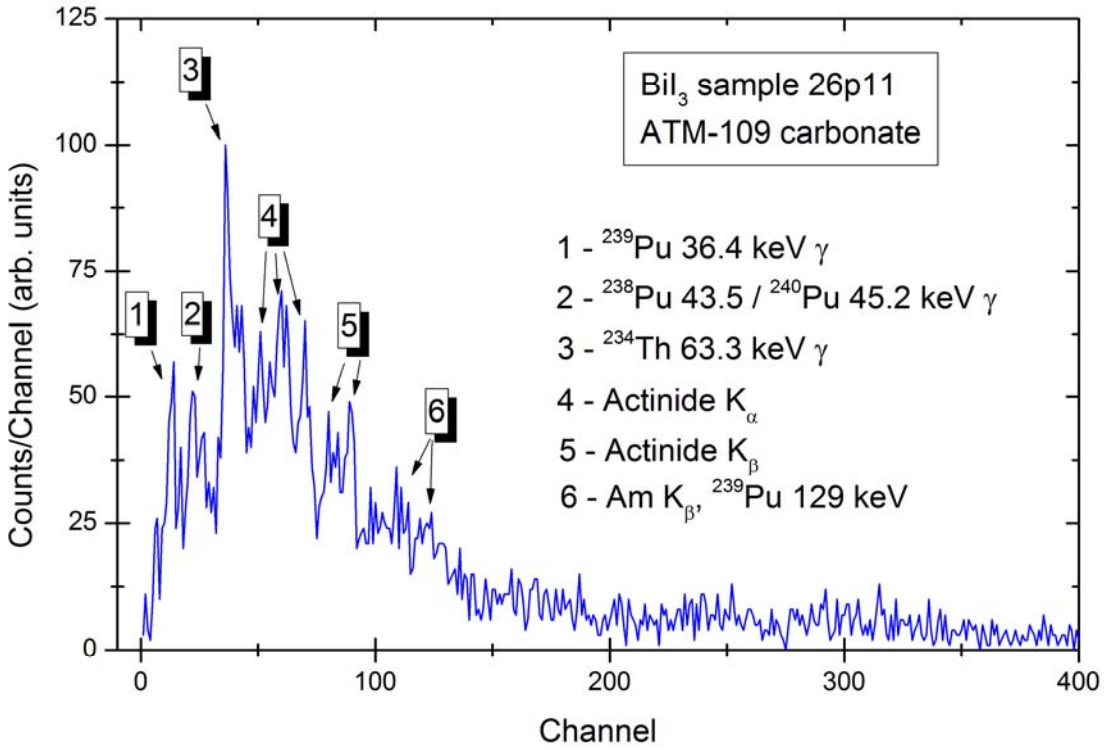

Figure 42. Gamma ray spectrum obtained from a BiI_3 spectrometer from spent fuel source 109-HBU carbonate.

Apart from spent fuel comparisons, it is useful to judge the theoretical efficiency of BiI_3 compared with other RTSD compounds. A comparison of the simulated gamma ray spectra from a ^{137}Cs source as obtained from BiI_3, HgI_2, TlBr, and CZT is presented in Figure 43. Each detector simulated in Figure 43 was resolution broadened to 4%. The photopeak efficiency is an important

property for a gamma ray detector, and represents the ratio of full-energy deposition events that occur through the photoelectric effect to those which occur in Compton interactions, pair production interactions, or inelastic scatter. In comparing the four RTSD compounds in Figure 43, the 662 keV photopeak efficiency of BiI_3, 16.8%, is second only to that of HgI_2 at 19.3% [51].

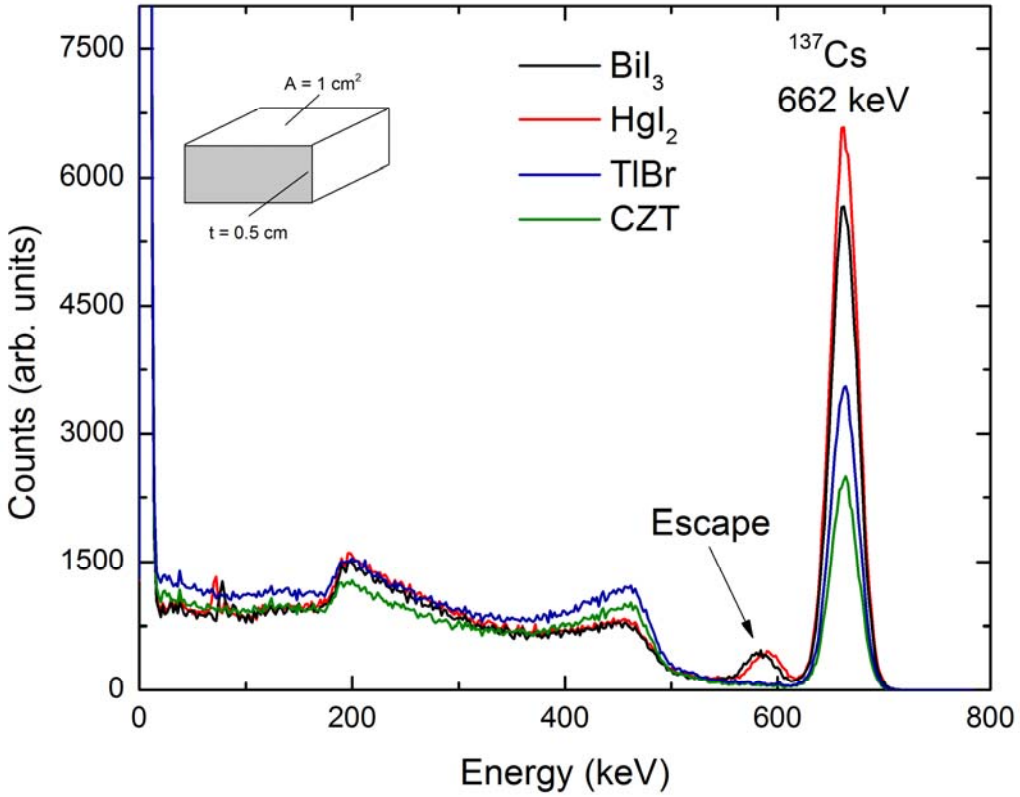

Figure 43. Simulated comparison of spectra obtained from a ^{133}Cs source with CZT, TlBr, HgI_2, and BiI_3 sensors. Simulation performed in MCNP6 with 4% Gaussian energy broadening applied to the photopeak.

Objective 13: Measure and Compare Plutonium and Uranium Standards

Samples of pure U and Pu were not readily available for testing in this work, however, the spent fuel study shows the primary signatures from high burnup fuels containing a mixture of U and Pu based oxides.

List of Publications and Presentations

Ph.D. Dissertation

Paul M. Johns, “Materials Development for Nuclear Security: Bismuth Triiodide Room Temperature Gamma Ray Sensors”, University of Florida, Gainesville FL (2017).

Papers

Paul M. Johns, James E. Baciak, Juan C. Nino, “Enhanced Gamma Ray Sensitivity in BiI_3 Sensors through Volumetric Defect Control”, *Applied Physics Letters* 109, 092105 (2016).

Paul M. Johns, Soumitra Sulekar, Shinyoung Yeo, Mary Bliss, James E. Baciak, Juan C. Nino, “Superheating Suppresses Structural Disorder in Sb-Doped BiI_3 Grown by the Bridgman Method”, *Journal of Crystal Growth*, 433, 153-159 (2015).

Paul M. Johns, Mary Bliss, Juan C. Nino “Sb:BiI_3 – Developing the Next Room Temperature Spectrometer”, *Transactions of the American Nuclear Society*, 2015 ANS Winter Meeting and Nuclear Technology Expo (2015).

Soumitra Sulekar, Beverly Brooks-Hinojosa, Paul M. Johns, Juan C. Nino, “Adsorption and Interaction of Au, Pt, and Pd on BiI_3 (001) Surfaces through Density Functional Theory Simulations” *Physical Chemistry Chemical Physics* (Submitted, 2017).

Presentations

Paul M. Johns, E. E. Wong, James E. Baciak, Juan C. Nino, "Sb:BiI_3 Detectors for Safeguards Applications", Institute of Nuclear Materials Management 2016 Meeting, Atlanta GA (2016).

Paul M. Johns, James E. Baciak, Juan C. Nino, "Investigating Spectral Response From High Quality Sb:BiI_3 Crystals," IEEE Symposium on Radiation Measurement and Applications (SORMA), Berkeley CA (2016).

Paul M. Johns, Mary Bliss, Juan C. Nino "Sb:BiI_3 - Developing the Next Room Temperature Spectrometer," American Nuclear Society Winter Meeting, Washington D.C. (2015).

Juan C. Nino, Paul M. Johns, James E. Baciak "Structural Improvements Yield Enhanced Gamma Ray Sensitivity in Sb-Doped BiI_3," IEEE Nuclear Science Symposium, San Diego CA (2015).

J. C. Nino, Paul M. Johns, Kelly Jordan, Mary Bliss, James Baciak "Defect Engineering and Growth of Sb:BiI_3 for Enhanced Nuclear Radiation Semiconductor Detectors", American Conference on Crystal Growth and Epitaxy, Big Sky MT (2015).

Paul M. Johns, HyukSu Han, Mary Bliss, Juan C. Nino, "Advancements in $Bi_xSb_{1-x}I_3$ Single Crystals for Ambient Temperature Gamma Detection" American Nuclear Society Winter Meeting and Nuclear Technology Expo, Anaheim CA (2014).

References

1. Qiu, W., *Growth and characterization of bismuth tri-iodide single crystals by modified vertical Bridgman method*. 2010, Gainesville, FL: University of Florida.
2. Johns, P.M., et al., *Superheating Suppresses Structural Disorder in Layered BiI_3 Semiconductors Grown by the Bridgman Method.* Journal of Crystal Growth, 2015.
3. Andreini, J.C.K., et al. *CZT sub-surface damage assessment using electrical leakage measurements*. in *2009 IEEE Nuclear Science Symposium Conference Record (NSS/MIC)*. 2009.
4. Bliss, M., et al., *Pb quantification of CdZnTe microheterogeneities complimented by SEM, IR microscopy, EDX, and TOF-SIMS.* Nuclear Instruments and Methods in Physics Research Section A: Accelerators, Spectrometers, Detectors and Associated Equipment, 2007. **579**(1): p. 138-140.
5. Bolotnikov, A.E., et al., *Extended Defects in CdZnTe Radiation Detectors.* Ieee Transactions on Nuclear Science, 2009. **56**(4): p. 1775-1783.
6. Duff, M., et al., *Characterization of heterogeneities in detector-grade CdZnTe crystals.* Journal of Materials Research, 2009. **24**(04): p. 1361-1367.
7. Xu, L.Y., et al., *Effects of Crystal Growth Methods on Deep-Level Defects and Electrical Properties of CdZnTe:In Crystals.* Journal of Electronic Materials, 2015. **44**(1): p. 518-523.
8. Triboulet, R. and P. Siffert, *CdTe and Related Compounds; Physics, Defects, Hetero- and Nano-structures, Crystal Growth, Surfaces and Applications: Physics, CdTe-based Nanostructures, CdTe-based Semimagnetic Semiconductors, Defects*. 2009: Elsevier Science.
9. Rudolph, P., et al., *The crystal perfection depends on the superheating of the mother phase too - Experimental facts and speculations on the "melt structure" of semiconductor compounds.* Journal of Crystal Growth, 1996. **166**(1-4): p. 578-582.
10. Saucedo, E., P. Rudolph, and E. Dieguez, *Modified Bridgman growth of CdTe crystals.* Journal of Crystal Growth, 2008. **310**(7-9): p. 2067-2071.
11. Weise, S., M. Salk, and V. Kramer, *Growth of twin free $AgGaS_2$ single crystals using a modified gradient freezing technique*, in *Ternary and Multinary Compounds*, R.D. Tomlinson, A.E. Hill, and R.D. Pilkington, Editors. 1998, Iop Publishing Ltd: Bristol. p. 111-114.

12. Chevy, A., *Segregation of dopants in melt-grown indium selenide crystals.* Journal of Applied Physics, 1984. **56**(4): p. 978-982.
13. Szeles, C., *CdZnTe and CdTe materials for X-ray and gamma ray radiation detector applications.* physica status solidi (b), 2004. **241**(3): p. 783-790.
14. Wright, G., et al., *The effects of chemical etching on the charge collection efficiency of {111} oriented Cd0.9Zn0.1Te nuclear radiation detectors.* IEEE Transactions on Nuclear Science, 2002. **49**(5): p. 2521-2525.
15. Levi, A., M.M. Schieber, and Z. Burshtein, *Carrier surface recombination in HgI2 photon detectors.* Journal of Applied Physics, 1983. **54**(5): p. 2472-2476.
16. Oliveira, I.B., et al., *Influence of crystalline surface quality on TlBr radiation detector performance.* IEEE transactions on nuclear science, 2005. **52**(5): p. 2058-2062.
17. Gokhale, S.H., HyukSu; Jordan, Kelly; Nino, Juan C.; Baciak, J.E., *Fabrication and Testing of Antimony Doped Bismuth Tri-Iodide Semiconductor Gamma-Ray Detectors.* Submitted to Nuclear Insurumentation and Methods A, 2015.
18. Chiu, F.-C., *A review on conduction mechanisms in dielectric films.* Advances in Materials Science and Engineering, 2014. **2014**.
19. Qiu, W., et al., *Interfacial Reactivity of Au, Pd, and Pt on BiI3 (001): Implications for Electrode Selection.* Acs Applied Materials & Interfaces, 2011. **3**(6): p. 1910-1917.
20. Dmitriyev, Y.N., et al. *Bismuth iodide crystals as a detector material: some optical and electrical properties*. 1999.
21. Saito, T., et al., *BiI3 single crystal for room-temperature gamma ray detectors.* Nuclear Instruments and Methods in Physics Research Section A: Accelerators, Spectrometers, Detectors and Associated Equipment, 2016. **806**: p. 395-400.
22. Gokhale, S.S., et al., *Growth, fabrication, and testing of bismuth tri-iodide semiconductor radiation detectors.* Radiation Measurements, 2015. **74**(0): p. 47-52.
23. Podraza, N.J., et al., *Band gap and structure of single crystal BiI3: Resolving discrepancies in literature.* Journal of Applied Physics, 2013. **114**(3).
24. Lintereur, A.T., et al., *Characterization of bismuth tri-iodide single crystals for wide band-gap semiconductor radiation detectors.* Nuclear Instruments and Methods in Physics Research Section A: Accelerators, Spectrometers, Detectors and Associated Equipment, 2011. **652**(1): p. 166-169.
25. Han, H., et al., *Defect Engineering of BiI3 Single Crystals: Enhanced Electrical and Radiation Performance for Room Temperature Gamma-Ray Detection.* Journal of Physical Chemistry C, 2014. **118**(6): p. 3244-3250.
26. Johns, P.M., J.E. Baciak, and J.C. Nino, *Enhanced gamma ray sensitivity in bismuth triiodide sensors through volumetric defect control.* Applied Physics Letters, 2016. **109**(9): p. 092105.
27. Gokhale, S., *Bismuth Triiodide Radiation Detector Development*, in *Nuclear Engineering*. 2015, University of Florida: Gainesville, FL.
28. *Bismuth triiodide (BiI3) optical properties, dielectric constant, non-linear properties*, in *Non-Tetrahedrally Bonded Elements and Binary Compounds I*, O. Madelung, U. Rössler, and M. Schulz, Editors. 1998, Springer Berlin Heidelberg: Berlin, Heidelberg. p. 1-7.
29. Levi, A., M.M. Schieber, and Z. Burshtein, *Dark current transients in HgI2 single crystals used as γ- and x-ray spectrometers.* Journal of Applied Physics, 1985. **57**(6): p. 1944-1950.
30. Gokhale, S.S., et al., *Growth, fabrication, and testing of bismuth tri-iodide semiconductor radiation detectors.* Radiation Measurements, 2015. **74**: p. 47-52.
31. Gokhale, S.S., et al., *Fabrication and testing of antimony doped bismuth tri-iodide semiconductor gamma-ray detectors.* Radiation Measurements, 2016. **91**: p. 1-8.
32. Edwards, N.S. and D.S. McGregor, *Charge Collection Efficiency Mapping of a Frisch-Collared BiI3 Device.*

33. Karban, P., et al., *Numerical solution of coupled problems using code Agros2D.* Computing, 2013. **95**(1): p. 381-408.
34. Barrett, H.H., J.D. Eskin, and H.B. Barber, *Charge Transport in Arrays of Semiconductor Gamma-Ray Detectors.* Physical Review Letters, 1995. **75**(1): p. 156-159.
35. Baciak, J.E. and Z. He, *Comparison of 5 and 10 mm thick HgI2 pixelated γ-ray spectrometers.* Nuclear Instruments and Methods in Physics Research Section A: Accelerators, Spectrometers, Detectors and Associated Equipment, 2003. **505**(1–2): p. 191-194.
36. Baciak, J.E. and H. Zhong, *Spectroscopy on thick HgI2 detectors: a comparison between planar and pixelated electrodes.* Nuclear Science, IEEE Transactions on, 2003. **50**(4): p. 1220-1224.
37. Baciak, J.E. and H. Zhong, *Long-term stability of 1-cm thick pixelated HgI_2 gamma-ray spectrometers operating at room temperature.* IEEE Transactions on Nuclear Science, 2004. **51**(4): p. 1886-1894.
38. Bolotnikov, A.E., et al., *Charge loss between contacts of CdZnTe pixel detectors.* Nuclear Instruments and Methods in Physics Research Section A: Accelerators, Spectrometers, Detectors and Associated Equipment, 1999. **432**(2–3): p. 326-331.
39. Hansson, C.C.T., et al., *Synchrotron radiation studies of spectral response features caused by Te inclusions in a large volume coplanar grid CdZnTe detector.* Nuclear Instruments and Methods in Physics Research Section A: Accelerators, Spectrometers, Detectors and Associated Equipment, 2012. **695**: p. 283-287.
40. Szeles, C., et al. *Fabrication of high performance CdZnTe quasi-hemispherical gamma-ray CAPture™ plus detectors*.
41. Kazyrevich, M., et al., *Photocurrent switching effect on platelet-like BiOI electrodes: influence of redox system, light wavelength and thermal treatment.* Electrochimica Acta, 2016. **190**: p. 612-619.
42. Fang, M., et al., *Construction of flexible photoelectrochemical solar cells based on ordered nanostructural BiOI/Bi 2 S 3 heterojunction films.* Physical Chemistry Chemical Physics, 2015. **17**(20): p. 13531-13538.
43. *Characterization of Spent Fuel Approved for Testing (ATM-109)*. 1998, Pacific Northwest National Lab., Richland, WA (United States).
44. Hanson, B., et al., *Analysis of High-Burnup and MOx Fuel for Inclusion in International Spent Fuel Databases*. 2012, Pacific Northwest National Lab., Richland, WA (United States).
45. Rodriguez, D.C., et al., *Measurement and analysis of gamma-rays emitted from spent nuclear fuel above 3MeV.* Applied Radiation and Isotopes, 2013. **82**: p. 181-187.
46. Orton, C.R., et al., *Proof of concept experiments of the multi-isotope process monitor: An online, nondestructive, near real-time monitor for spent nuclear fuel reprocessing facilities.* Nuclear Instruments and Methods in Physics Research Section A: Accelerators, Spectrometers, Detectors and Associated Equipment, 2012. **672**: p. 38-45.
47. Reilly, D., et al., *Passive nondestructive assay of nuclear materials*. 1991, Nuclear Regulatory Commission, Washington, DC (United States). Office of Nuclear Regulatory Research; Los Alamos National Lab., NM (United States).
48. Quam, W., *Cadium-Zinc-Telluride (CZT) Gamma Ray Spectrometry*. 2001, Bechtel Nevada Corporation (US).
49. Manini, H., *Simulation and Comparison of Various Gamma-Ray Imaging Detector Configurations for IPRL Devices*. 2006.
50. Fast, J.E., et al., *Spent Nuclear Fuel Measurements*. 2014, Pacific Northwest National Laboratory (PNNL), Richland, WA (US).
51. Lintereur, A.T., et al. *Iodine based compound semiconductors for room temperature gamma-ray spectroscopy*. 2008.